Dynamic fracturing by successive coseismic loadings leads to pulverization in active fault zones

Frans F M Aben, M.-L Doan, Thomas Mitchell, R Toussaint, T Reuschlé, Michele Fondriest, J.-P Gratier, F Renard

▶ **To cite this version:**

Frans F M Aben, M.-L Doan, Thomas Mitchell, R Toussaint, T Reuschlé, et al.. Dynamic fracturing by successive coseismic loadings leads to pulverization in active fault zones. Journal of Geophysical Research : Solid Earth, 2016, 121, pp.23. 10.1002/2015JB012542 . hal-01304634

HAL Id: hal-01304634
https://hal.science/hal-01304634v1

Submitted on 20 Apr 2016

HAL is a multi-disciplinary open access archive for the deposit and dissemination of scientific research documents, whether they are published or not. The documents may come from teaching and research institutions in France or abroad, or from public or private research centers.

L'archive ouverte pluridisciplinaire **HAL**, est destinée au dépôt et à la diffusion de documents scientifiques de niveau recherche, publiés ou non, émanant des établissements d'enseignement et de recherche français ou étrangers, des laboratoires publics ou privés.

AGU PUBLICATIONS

JGR

Journal of Geophysical Research: Solid Earth

RESEARCH ARTICLE
10.1002/2015JB012542

Key Points:
- Experimental dynamic fracturing can lead to pulverization through multiple high-strain rate loadings with moderate stress
- Successive transient loadings decrease the pulverization strain rate threshold
- Consecutive seismic events cause progressive broadening of the band of pulverized rocks in a fault damage zone

Supporting Information:
- Supporting Information S1

Correspondence to:
F. M. Aben,
franciscus.aben@univ-grenoble-alpes.fr

Citation:
Aben, F. M., M.-L. Doan, T. M. Mitchell, R. Toussaint, T. Reuschlé, M. Fondriest, J.-P. Gratier, and F. Renard (2016), Dynamic fracturing by successive coseismic loadings leads to pulverization in active fault zones, *J. Geophys. Res. Solid Earth*, *121*, doi:10.1002/2015JB012542.

Received 22 SEP 2015
Accepted 28 MAR 2016
Accepted article online 2 APR 2016

©2016. The Authors.
This is an open access article under the terms of the Creative Commons Attribution License, which permits use, distribution and reproduction in any medium, provided the original work is properly cited.

Dynamic fracturing by successive coseismic loadings leads to pulverization in active fault zones

F. M. Aben[1,2], M.-L. Doan[1,2], T. M. Mitchell[3], R. Toussaint[4], T. Reuschlé[4], M. Fondriest[5], J.-P. Gratier[1,2], and F. Renard[1,2,6]

[1]University Grenoble Alpes, ISTerre, Grenoble, France, [2]CNRS, ISTerre, Grenoble, France, [3]Department of Earth Sciences, University College London, London, UK, [4]Institut de Physique du Globe de Strasbourg, University of Strasbourg/EOST, Strasbourg, France, [5]School of Earth, Atmospheric and Environmental Sciences, University of Manchester, Manchester, UK, [6]PGP, Department of Geosciences, University of Oslo, Oslo, Norway

Abstract Previous studies show that pulverized rocks observed along large faults can be created by single high-strain rate loadings in the laboratory, provided that the strain rate is higher than a certain pulverization threshold. Such loadings are analogous to large seismic events. In reality, pulverized rocks have been subject to numerous seismic events rather than one single event. Therefore, the effect of successive "milder" high-strain rate loadings on the pulverization threshold is investigated by applying loading conditions below the initial pulverization threshold. Single and successive loading experiments were performed on quartz-monzonite using a Split Hopkinson Pressure Bar apparatus. Damage-dependent petrophysical properties and elastic moduli were monitored by applying incremental strains. Furthermore, it is shown that the pulverization threshold can be reduced by successive "milder" dynamic loadings from strain rates of ~180 s^{-1} to ~90 s^{-1}. To do so, it is imperative that the rock experiences dynamic fracturing during the successive loadings prior to pulverization. Combined with loading conditions during an earthquake rupture event, the following generalized fault damage zone structure perpendicular to the fault will develop: furthest from the fault plane, there is a stationary outer boundary that bounds a zone of dynamically fractured rocks. Closer to the fault, a pulverization boundary delimits a band of pulverized rock. Consecutive seismic events will cause progressive broadening of the band of pulverized rocks, eventually creating a wider damage zone observed in mature faults.

1. Introduction

Upper crustal fault zones typically consist of a fault core and a surrounding fracture damage zone. The fault core consists of highly damaged comminuted fault rock that accommodates most of the cumulative fault slip, while the surrounding fracture damage zone accumulates fracture damage without or with only slight displacement [*Faulkner et al.*, 2003]. The changes in properties of the fault damage zone rocks (such as rock stiffness and permeability) with respect to the protolith have a direct effect on the mechanics of faulting during the different stages of the seismic cycle [e.g., *Bruhn et al.*, 1994; *Faulkner et al.*, 2006; *Griffith et al.*, 2012]. Such changes include fault creep by fluid-driven mineralogical changes occurring over longer periods of time [e.g., *Lockner et al.*, 2011; *Moore and Rymer*, 2012] and postseismic creep by pressure solution that is enhanced in fault damage zones by a higher fracture surface area [*Gratier et al.*, 2013a, 2013b].

Also, the fault damage zone has direct effects on the dynamics of earthquake rupture propagation. This includes increasing the amount of energy dissipation [e.g., *Andrews*, 2005], changing the efficiency of weakening mechanisms such as thermal pressurization of pore fluids [e.g., *Noda and Lapusta*, 2013], influencing rupture directivity [e.g., *Ampuero and Ben-Zion*, 2008; *Huang and Ampuero*, 2011; *Cappa et al.*, 2014; *Huang et al.*, 2014], and even generating seismic waves by off-fault damage [*Ben-Zion and Ampuero*, 2009]. Therefore, it is crucial to characterize the temporal and spatial changes in damage in fault damage zones.

This paper focuses on damage generation produced by earthquake ruptures (i.e., coseismic damage). Coseismic damage is induced by transient loading conditions due to the propagation of stress waves at the earthquake rupture tip. The associated inertia effects influence the mechanical properties of the rock, such as an increase in peak strength and fracture toughness [*Kolsky*, 1949; *Bhat et al.*, 2012; *Zhang and Zhao*, 2013]. Consequently, this causes dynamic fracturing that affects both the propagation of individual fractures [*Fineberg et al.*, 1991; *Sharon and Fineberg*, 1999] and their elastic interactions, such as stress shadowing. This suggests that for the

same stress conditions, significantly more damage can be induced and more energy dissipated at higher strain rates. Therefore, coseismic damage is an important piece of the puzzle regarding the energy budget of rupture events [*Scholz*, 2002] since the elastic strain energy released during the rupture event is dissipated into new fracture damage. Current estimates for dissipated fracture energy within the damage zone range from 1% [*Rockwell et al*., 2009] to 50% [*Wilson et al*., 2005]of the total energy budget.

Pulverized rocks are thought to be the most extreme case of coseismic dynamic fracturing. These rocks are found from several tens to hundreds of meters from the fault core [*Dor et al*., 2006b; *Mitchell et al*., 2011; *Rempe et al*., 2013] and are characterized by very low shear strain and a very high fracture density at or below the grain scale. Laboratory single-impact high-loading rate experiments in compression reveal that pulverization, commonly defined from a macroscopic description of when samples broke/disintegrated into a myriad of fragments, takes place above a certain strain rate threshold [*Xia et al*., 2008; *Doan and Gary*, 2009; *Yuan et al*., 2011; *Doan and d'Hour*, 2012] or a certain strain threshold [*Doan and Billi*, 2011]. Such pulverization thresholds in combination with field observations provide a unique opportunity to determine transient loading conditions. For instance, loading conditions produced by a subshear velocity rupture prove to be insufficient for pulverization at distances of a few meters to hundreds of meters from the fault [*Doan and Gary*, 2009]. Therefore, several authors suggest that supershear ruptures, and the shock waves they produce, may be responsible for the loading conditions needed for pulverization at these distances from the fault core [*Doan and Gary*, 2009; *Wechsler et al*., 2011; *Yuan et al*., 2011; *Rowe and Griffith*, 2015]. Near some faults, pulverized rocks have an asymmetric distribution across the fault, suggesting that bimaterial ruptures are causing the loading conditions needed for pulverization, although in this particular case pulverization occurs during tensile loading or a stress drop [*Ben-Zion and Shi*, 2005; *Dor et al*., 2006b; *Mitchell et al*., 2011].

However, pulverized rocks in nature have experienced numerous coseismic loadings, and therefore, the comparison of field data with single-loading experiments cannot be made directly. This work therefore investigates incremental weakening and pulverization by successive seismic events (i.e., multiple impacts/loadings), as suggested by *Doan and D'Hour* [2012]. Incremental weakening successive loadings at intermediate strain rate have been performed previously on granite by *Li et al.* [2005] for geotechnical purposes, but our study extends their work by focussing on pulverization, providing petrophysical and microstructural studies of damage, and by applying our results to active faults.

To study the effect of successive "milder" high-strain rate loadings, compressive dynamic loading experiments were performed on a series of quartz-monzonite samples using a Split Hopkinson Pressure Bar (SHPB) apparatus [*Kolsky*, 1949; *Chen and Song*, 2010]. One series of samples underwent a variable amount of successive loading impacts. A second series of samples was subjected to single loadings with higher loading rates and stresses. Damage was monitored between successive loadings using several proxies (porosity and Brunauer-Emmett-Teller (BET) surface area measurements and ultrasonic wave velocities). Postloading microstructures were studied by optical microscopy, scanning electron microscopy (SEM), and X-ray computed tomography (CT) imaging.

The results show first of all that pervasive dynamic fracturing occurs in the "macroscopically intact" and predamaged rocks. Certain distinctive features in the mechanical data were then used to define pulverization from dynamic fracturing in the experiments. It is then possible to establish the pulverization thresholds (strain rate and strain) for the single and successive loadings series and subsequently discuss their changes with time. Finally, the conditions for dynamic fracturing and pulverization are integrated in a conceptual model to discuss the effect of successive high-strain rate loadings on changes in fault zone damage (such as decrease in elastic constants), and the constraints they give on the earthquake rupture mechanism and on the dissipated fracture energy. It is hoped that this will contribute to earthquake slip and damage models [e.g., *Bhat et al*., 2007, 2012; *Xu and Ben-Zion*, 2013; *Cappa et al*., 2014; *Johri et al*., 2014] and motivate new field studies on pulverized rocks.

2. Materials and Methods

2.1. High-Strain Rate Experiments

The high-strain rate experiments were performed with a calibrated "mini-Split Hopkinson Pressure Bar" ("mini-SHPB") apparatus custom built at the ISTerre laboratory in Grenoble (Figure 1a). The SHPB is a loading apparatus that transmits planar elastic compressive waves into a solid sample. It consists of a launching mechanism and an input bar (1.5 m length) and an output bar (1 m length), both of which are 2 cm in diameter (Figure 1b).

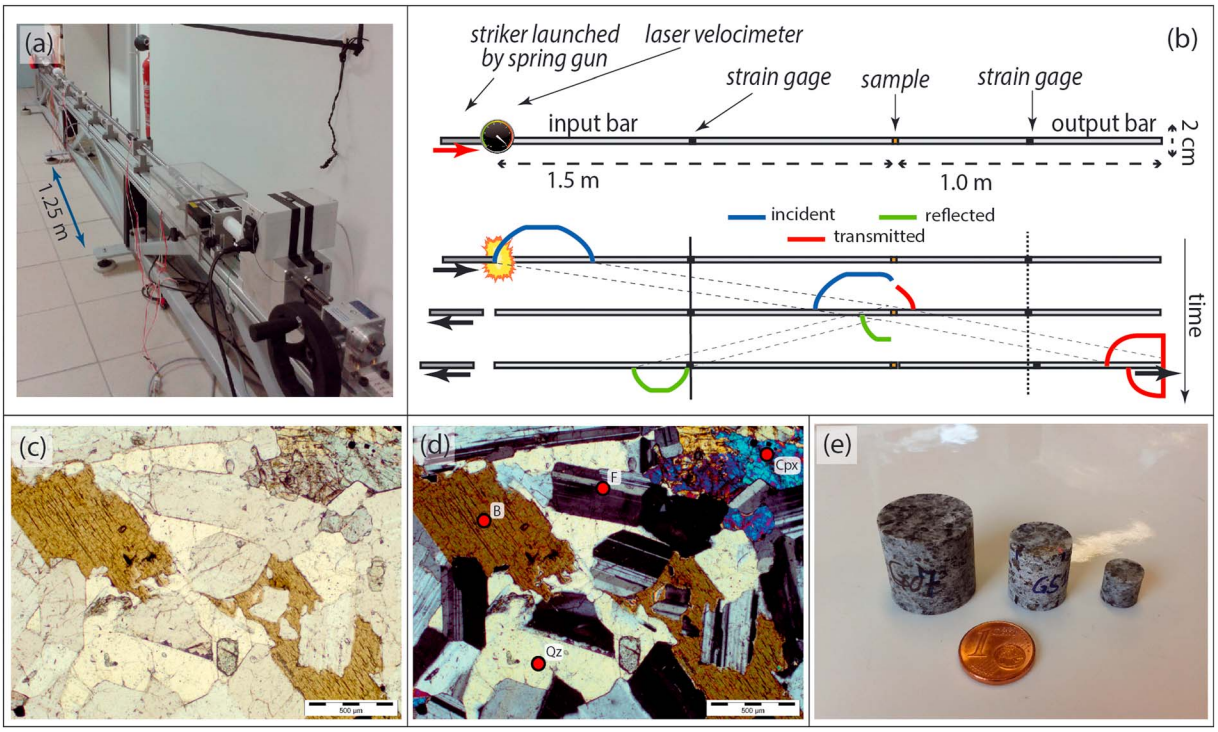

Figure 1. (a) Photograph of the mini-SHPB apparatus. (b) Sketch of the mini-Split Hopkinson Pressure Bar at the ISTerre laboratory in Grenoble. The velocimeter records the speed of the striker bar and triggers the acquisition system. Note that the output bar is shorter than the input bar. Strain gauges (Kyowa type KFG-2-120-D1-11L1M2S) record the incident (blue), reflected (green), and transmitted (red) stress waves as they travel along the length of the bars as indicated by the three time snapshots. (c, d) Microphotographs of intact quartz-monzonites taken with parallel polarizers (Figure 1c) and crossed polarizers (Figure 1d). B = biotite, Qz = quartz, F = feldspar, Cpx = clinopyroxene. (e) Different-sized quartz-monzonite samples used for the experiments.

The samples were placed between both bars and held in place by a small amount of high-vacuum grease, covering the whole sample surface. A soft isolation material and a thin plastic sheet wrapped around the sample prevented postloading damage since the sample detaches from the setup after loading.

A steel striker that is launched by a spring gun (maximum muzzle velocity 4.5 ms^{-1}) toward the input bar generates a compressive stress wave on impact. This incident wave loads the sample when it has traveled along the length of the input bar (Figure 1b). During loading, part of the incident wave is reflected back toward the beginning of the setup. Part of the stress wave is transmitted to the output bar (Figure 1b). Strain gages are placed at the middle of the input and output bars to record the incident, reflected and transmitted waves. The complete stress-strain history is computed from the recorded data by applying a 1-D wave analysis. For an extensive overview of the 1-D wave analysis, the preprocessing of the data, and the assumptions and requirements needed for a reliable test, the reader is referred to supporting information S1 or to *Graff* [1991]; *Gama et al.* [2004]; *Chen and Song* [2010] and *Zhang and Zhao* [2013].

Experiments were performed on quartz-monzonite samples cored from a single block. The rock consists of 17.9% quartz, 12.8% biotite, 57.6% plagioclase (38% An), and 11.7% clinopyroxene and other minor minerals (Figures 1c and 1d). The mean grain size is 450 μm. Initial porosity is 0.78 ± 0.3%. The mechanical parameters of the rock (Young's modulus and Poisson's ratio) were determined by uniaxial compression tests (see section 2.2). Quartz-monzonites are similar in mineral composition and structure to granitic rocks tested in other studies [*Li et al.*, 2005; *Xia et al.*, 2008; *Doan and Gary*, 2009; *Yuan et al.*, 2011; *Doan and D'Hour*, 2012], but thanks to the smaller grain size, it is possible to use smaller sample sizes.

Three sets of cylindrical samples of ~10 mm, ~15 mm, and ~20 mm diameters (Figure 1e) labeled GT#, GS#, and G, respectively, were tested at different stress levels (Table 1). The length/diameter ratio was close to 1 to eliminate radial and axial inertia effects (see supporting information S1). One set of samples was loaded

Table 1. Overview of Samples Used for High Strain Rate Testing Including Test Settings[a]

Sample nr	Diameter (mm)	Length (mm)	Striker Length (cm)	Spring Displacement (cm)	Pulse Shaper	Number of Loadings	Porosity	*P* wave Velocity	*S* Wave Velocity (Axial)	BET	Microstructural Study	UCS
G01	19.46	20.00	20	5	no	37						
G09	19.46	20.02	20	5.5	no	12	X	axial, radial				
G10	19.45	20.00	20	5.5	no	30	X	axial, radial				
G11	19.44	20.02	20	5.5	no	40	X	axial, radial				
G13	19.44	19.98	20	5.5	no	10		axial, radial				
GS01	14.64	17.14	20	5	no	4				X		
GS02	14.64	16.70	15	5.5	no	4		axial	X	X	X-ray μCT	
GS03	14.64	17.36	15	5.5	no	3	X	axial, radial	X	X		
GS04	14.62	17.20	15	5.5	no	4	X			X		
GS05	14.65	16.74	15	5.5	no	2	X	axial, radial	X			
GS07*	14.50	17.01	15	5.5	no	3	X	axial, radial		X		
GS11	14.90	14.24	20	5.5	yes	6						
GS12	14.88	14.70	20	5.5	yes	3						UCS
GS13	14.93	14.75	20	5.5	yes	4						UCS
GS14	14.92	14.55	20	5.5	yes	2						UCS
GT01	10.60	9.58	15	5.5	yes	1						
GT03	9.80	9.27	15	5.5	yes	1						
GT04	9.60	9.26	10	4.0	yes	1				X		
GT05	8.82	9.24	20	5.5	yes	1						
GT06	8.88	9.76	20	5.5	yes	1						
GT08	8.94	7.86	20	5.0	yes	1				X		
GT09	8.90	8.50	20	5.5	yes	1		*plastic jacket*			thin section	
GT10	8.90	8.40	20	5.5	yes	1		*plastic jacket*			thin section	
initial state	-	-	-	-	-	0	X	axial, radial	X	X	thin section	
UCS5	14.23	14.69	Uniaxial Compressive Strength Experiment					*Technical error during mechanical data acquisition: used data from sample GS02 to relate damage proxies*				
UCS6	14.65	14.82										
UCS7	32.80	14.65										
UCS8	30.20	14.79										

[a]Also indicated are the different damage proxies that have been measured. At the bottom are sample characteristics for the quasi-static compressive strength experiments.

once to obtain a similar data set to previous studies where loading rate was the changing parameter [*Doan and Gary*, 2009; *Doan and Billi*, 2011; *Yuan et al*., 2011; *Doan and D'Hour*, 2012]; the other samples were subjected to a varying number of successive loadings (Table 1). For some experiments, the strain rate was kept approximately the same by using cardboard pulse shapers to manipulate the shape of the incident wave and/or by applying different forces (expressed as the spring displacement, see Table 1). The pulse shapers were also applied if it was predicted that inelastic yielding would occur before stress equilibrium is reached. This prognosis was obtained by a stress equilibrium model based on elastic and acoustic parameters of the bar material and the rock (supporting information S1) [*Ravichandran and Subhash*, 1994]. A longer striker bar was used for larger samples or higher strains. The details of the samples, the number of loadings applied, and the specific SHPB settings are summarized in Table 1. All experiments were performed under dry conditions and at room temperature, close to 19°C ± 2°C.

2.2. Quasi-static Compressive Experiments

Uniaxial compressive strength (UCS) experiments (Table 1, bottom) were conducted on four samples to obtain quasi-static parameters (strength and elastic moduli) for comparison with the high-strain rate tests. The tests were performed at Institut de Physique du Globe de Strasbourg (IPGS)/Ecole et Observatoire des Sciences de la Terre (EOST) in Strasbourg using a Schenck Trebel uniaxial press. The applied strain rate was $5 \times 10^{-5}\,s^{-1}$. Two samples had a length/diameter ratio of ~1, similar to the dynamic testing samples. The other two samples had a standard dimension ratio of ~2.

UCS tests were applied to three samples that had already been subjected to a number of dynamic loadings on the SHPB apparatus (Table 1). These experiments were performed at University College London (UCL) in London on a SERVO Technique 20 ton uniaxial apparatus with a strain rate of $5 \times 10^{-5}\,s^{-1}$.

2.3. Damage Characterization

Damage characterization was performed on a set of samples (Table 1) that had been subjected to a different number of successive loadings so that it was not necessary to measure them after each individual loading. Damage was characterized by *P* and *S* wave velocity, porosity, BET specific surface area, X-ray computed tomography, and thin section analysis. The number of applied loads was used as a first comparative parameter between different samples. The second comparative parameter was dissipated energy (for computation, see supporting information S1), which eliminates differences between individual loadings and samples (e.g., applied peak stress and sample length). The individual damage proxies are detailed below.

2.3.1. Petrophysical Damage Characterization

The *P* wave velocities were measured at IPGS/EOST in Strasbourg, at ISTerre in Grenoble, and at UCL in London. Two methods were applied: (I) a standard approach to measure velocities along the sample axes using piezometer heads (700 kHz and 1 MHz frequency for measurements at IPGS/EOST and UCL, respectively) that are pressed to the sample with a stress of about 1 MPa or 0.5 MPa and (II) a less conventional method (Figure 2) using miniature piezometers (PAC micro-100S, frequency range 200–950 kHz). Here coupling was made by an acoustic echo fluid and low stress delivered by a small paint clamp. The mobile piezometers provided a means of measuring the velocities along and perpendicular to the sample axis, so that the damage anisotropy could be determined. Measurements were taken on the samples indicated in Table 1 and on four intact samples to establish initial-state *P* wave velocities as well. Error bars are 100 m/s (method I) and 150 m/s (method II).

S wave velocities were obtained on several samples (indicated in Table 1) at UCL in London with the same setup as that used for *P* wave velocity measurements. A similar stress of 0.5 MPa was applied to couple the *S* wave transducers (frequency range of 1 MHz) to the samples. Four separate measurements were taken on each sample, yielding error bars of 120 m/s. Poisson's ratio was calculated by using the *P* and *S* wave velocities measured at UCL.

Samples picked for porosity measurements (Table 1) were dried in a vacuum oven for a minimum of 12 h before the dry mass (m_{dry}) was measured. They were then placed under vacuum, and double-distilled water was added for imbibition. The samples stayed submerged for at least 12 h after which the saturated mass (m_{sat}) was measured. The Archimedes mass (m_{arch}) was obtained by measuring the mass of the sample while it was kept suspended and fully submerged in water. The porosity value (ϕ) was then obtained from

$$\varphi = \frac{m_{sat} - m_{dry}}{m_{sat} - m_{arch}} \times 100$$

The BET (Brunauer-Emmet-Teller) adsorption technique was applied on a set of samples (Table 1) to obtain the specific surface area. BET analyses were performed at EOST, Strasbourg, on a Sorptomatic 1990 apparatus and at ISTerre, Grenoble, on a BELSORP-max apparatus. Krypton was used as adsorption gas during the analysis, and the temperature was controlled by liquid nitrogen. The samples were pretreated by applying a vacuum for at least 12 h at temperatures of 40°C (Strasbourg BET) and 120°C (Grenoble BET) to remove excess gas and liquid components from the samples.

2.3.2. Microstructural Characterization

Images of the microstructure of damaged samples were obtained by X-ray microtomography and optical and scanning electron microscopy. Two X-ray microtomography scans were obtained on sample GS02 to monitor the differences in the fracture network between the third and fourth successive loadings. The scans were acquired with a laboratory-built X-ray computed tomography scanner at the 3S-R laboratory, University of Grenoble-Alpes. Voxel size was 11.8 μm, leading to a spatial resolution close to 24 μm. The data sets were analyzed using the software Avizo Fire for 3-D reconstruction and MATLAB for 2-D analysis. Porosity values were obtained from the 2-D and 3-D analyses; details of these calculations are presented in supporting information S2.

Thin sections were produced from the initial rock and from samples GT09 and GT10, parallel and perpendicular to the loading direction, respectively (see loading conditions in Table 1). Both optical microscopy and SEM analyses were performed on these thin sections. These two samples were jacketed with a piece of plastic tube (Tygon R3603, thickness 2 mm) that, compared to the samples, was of similar diameter and slightly shorter in length (~1 mm) to ensure that the in situ microstructures could be recovered after loading. Following the same approach as *Yuan et al.* [2011] and using the material properties of the Tygon tube, a confining stress of 2.3 MPa of the jacket on the sample was obtained. During radial expansion of the sample, the confining stress was possibly higher. Therefore, in order to maintain a conservative approach, these mechanical results were excluded from the discussion, although dynamic loading tests on Carrara marble did not show significantly

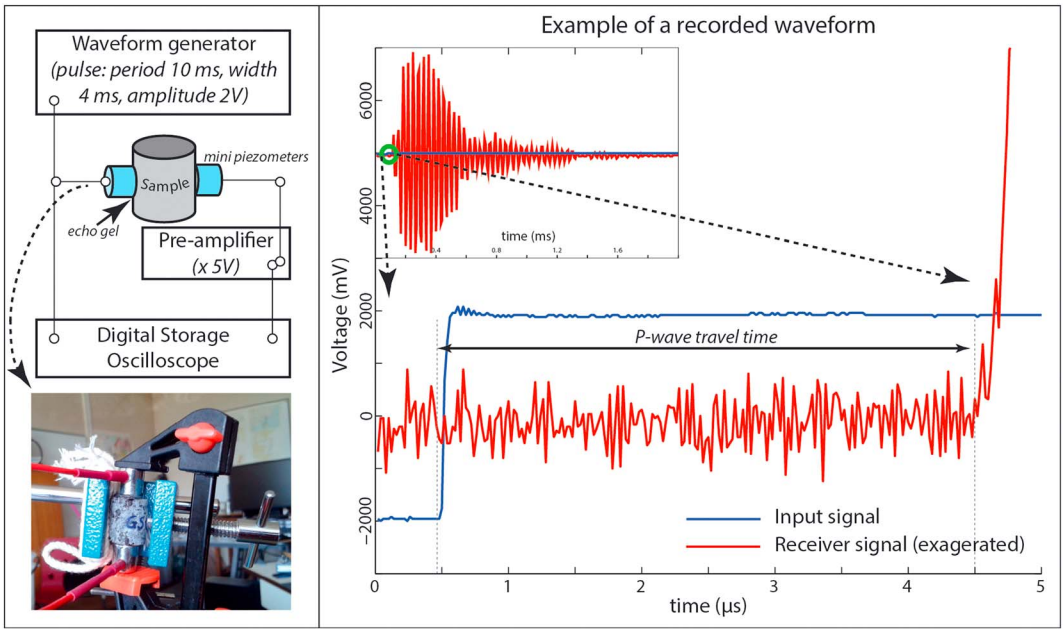

Figure 2. *P* and *S* wave velocity measurement method using minipiezometers. (top left) A sketch of the setup, including the properties of the generated pulse. An extra amplifier (Metrix AX502) placed before a digital storage oscilloscope (TENMA 72-8240 DSO) amplified the received signal. (bottom left) The attachment of the minipiezometers to the rock samples by a small paint clamp. (right) Example of a recorded waveform and the definitions of how the *P* wave travel time is picked.

different mechanical behavior between nonjacketed and jacketed samples [*Doan and Billi*, 2011]. It is worth noting that the axial stresses experienced by the samples are 2 orders of magnitude higher (220 MPa) than the confining stress of the jacket and that the microstructures represent the postfracturing state of the unconfined samples in which the flying away of fragments was avoided.

3. Results

3.1. Quasi-static Compressive Strength Tests

Samples UCS5 and UCS6, with dimension ratios of ~1, show a quasi-static peak strength of 196 MPa and 248 MPa, respectively. Samples UCS7 and UCS8 (dimension ratio 2) failed at 174 MPa and 209 MPa, respectively. These results show a wide scatter, possibly due to varying sample sizes, but display quasi-static strengths that can be expected for such rocks (e.g., UCS of Westerly granite = 200 MPa [*Lockner*, 1998]).

The predamaged samples GS14, GS12, and GS13 (dynamically loaded 2X, 3X, and 4X, respectively, see next section) give quasi-static peak strengths of 187, 181, and 149 MPa, respectively (Table 2).

3.2. Dynamic Compressive Loadings

3.2.1. Macroscopic Observations on Dynamically Loaded Samples

The different loading conditions, notably the applied stress (which is derived from the incident wave), resulted in different macroscopic failure modes (Table 2 and Figure 3). Samples loaded up to 100 MPa applied peak stress generally did not fail, or they failed after an arbitrary, but large, amount of successive loadings along a single fracture that appeared at around five loadings before full macroscopic failure (Figure 3a). Samples subjected to successive loadings with a higher applied stress (180–210 MPa) either failed into multiple fragments, often in the form of shards parallel to the loading direction (Figure 3b), or were pulverized (Figure 3c). Macroscopic failure by fragmentation or pulverization was observed after four to six successive loadings. Before that, visible damage appeared after the third successive loading. After majority of the first and second successive loadings, the samples looked apparently intact and undamaged. The smaller single-loading samples were split into multiple fragments at applied stresses below 315 MPa (Figure 3d). At higher applied stresses, they were labeled pulverized from a qualitative perspective: a large amount of the fragments seemed to be equal to or smaller than the original grain size (Figure 3e). A more quantitative mechanical definition for pulverization will be proposed later on (see section 4).

Table 2. Mechanical and Petrophysical Results[a]

	Number of Loadings	Applied Stress (MPa)	Macroscopic Failure Mode After Final Loading (Image No.)	Failure Mechanism Based on Mechanical Data	Porosity (%)	UCS (MPa)
G01	37	92–100	split	-		
G09	12	100–105	split (Figure 3b)	-	1.16	
G10	30	100–105	none	-	0.47	
G11	40	95–105	none	-	0.35	
G13	10	92–100	none	-		
GS01	4	180–183	pulverized (Figure 3f)	Pulverization		
GS02	4	188–208	multiple fragments[b]	Dynamic fracturing		
GS03	3	192–200	crack network visible	Dynamic fracturing	0.89	
GS04	4	200–208	multiple fragments (Figure 3c)	Dynamic fracturing	5.51	
GS05	2	200–203	none	Dynamic fracturing	0.83	
GS07[c]	3	-	crack network visible	Dynamic fracturing	1.63	
GS11	6	173–180	pulverized	Pulverization		
GS12	3	178–185	crack network visible	Dynamic fracturing		180.6
GS13	4	172–178	crack network visible	Dynamic fracturing		149.3
GS14	2	168–172	none	Dynamic fracturing		187.2
GT01	1	295	heavily fragmented	Dynamic fracturing		
GT03	1	313	heavily fragmented (Figure 3d)	Dynamic fracturing		
GT04	1	220	none	Dynamic fracturing		
GT05	1	400	pulverized	Pulverization		
GT06	1	500	pulverized	Pulverization		
GT08	1	440	pulverized (Figure 3e)	Pulverization		

[a]First column: number of loadings. Second column: applied peak stress, derived from the amplitude of the incident wave. Third column: macroscopic description of the damage. Fourth column: damage mechanism based on the definition for pulverization described in section 4. Fifth column: water porosity data. Sixth column: UCS obtained after dynamic loading.
[b]Electrical tape prevented loss of cohesion for damage proxy measurement..
[c]Technical error during mechanical data acquisition.

3.2.2. Mechanical Behavior of Dynamically Loaded Samples

The stress-strain-strain rate mechanical behavior of the samples was sorted into different classes. The proposed classes are characterized by the macroscopic end states: intact, damaged, fragmented, or pulverized. In contrast to conventional loading tests (such as UCS), the failure stress or strength of a sample during an SHPB test is not necessarily equal to the maximum stress of the input wave (the applied peak stress).

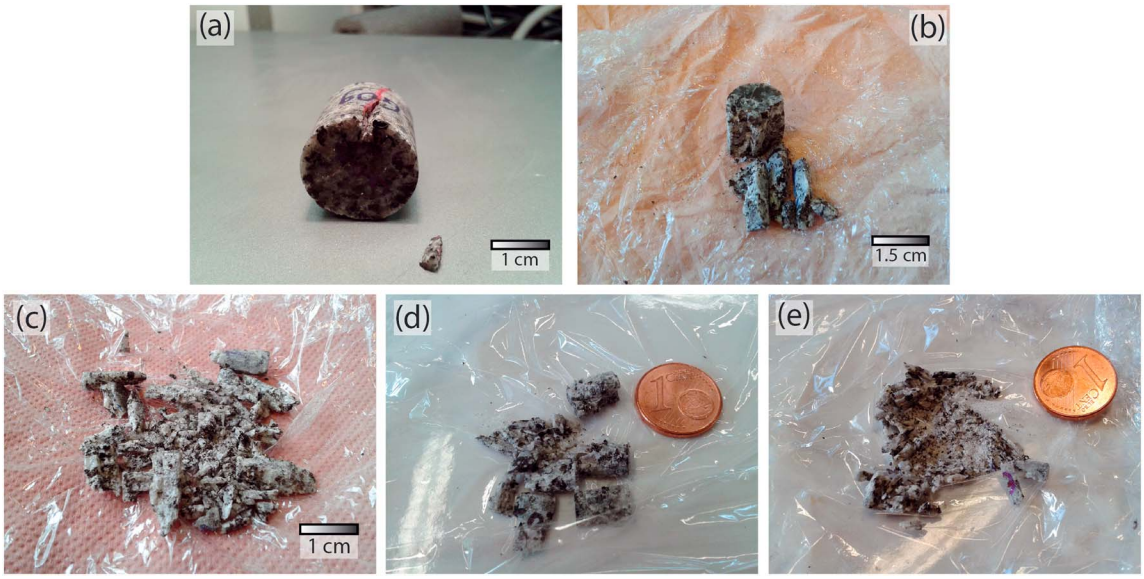

Figure 3. (a) Single fracture in sample G09 after 12 successive loadings at 100 MPa peak stress. (b) Fragmented sample GS04 after four successive loadings (peak stress 200–210 MPa). (c) Pulverized sample GS01 after four successive loadings (peak stress ~183 MPa). (d) Fragmented sample GT03 after a single loading (peak stress 313 MPa). (e) Pulverized sample GT08, loaded once at a peak stress of 440 MPa.

Therefore, both applied peak stress and strength are reported. Section 4 discusses the processes responsible for the different mechanical behaviors.

Mechanical class (I) (Figures 4a, 4b, and 4i) contains the intact and single-fractured samples loaded at ~100 MPa applied stress, well below the quasi-static peak strength. The loadings (>100 loadings on five samples, Table 2) experience a peak strain rate between 80 and 165 s^{-1} with a mean peak strain rate of 110 s^{-1}. The strain rate peaks occurs at half the peak stress and a decompressional peak strain rate (−80 s^{-1}) is observed at half the peak stress during unloading. In between these strain rate peaks, the samples deform under a relatively low constant strain rate (~10–15 s^{-1}) for a period of ~50 μs. The stress-strain curves indicate elastic behavior (Figure 4i). The residual strain and dissipated energy compensation values were derived from these loadings to correct for initial stress disequilibrium and grease and asperity deformation errors (see supporting information S1).

Class (II) encompasses single and successive loadings that were subject to an applied peak stress between 165 and 315 MPa and a peak strain rate between 115 and 200 s^{-1} (Figures 4c–4f and 4j). The strength of the samples varies but can be much lower than the applied peak stress, between 160 and 215 MPa. The residual strain varies between 0.01 and 1.2%. Furthermore, the stress and strain behavior is similar to class (I) with similar strain rate peaks during loading and unloading (Figures 4c–4e). In between these peaks, a "hick-up" or plateau with an average strain rate of 25–85 s^{-1} is observed. For loadings with higher residual strains (Figure 4f), this constant strain rate plateau is replaced by a continuously decreasing strain rate toward the decompressional strain rate peak. The macroscopic end state is either apparently intact (Figure 4c), with visible fractures (Figure 4d), or ranging from fragmented to nearly pulverized (Figures 4e and 4f).

Class (III) samples are qualitatively described as pulverized and have large corrected residual strains (1.2–3.7%) (Figures 4g, 4h, and 4k). Peak strengths vary between 200 and 250 MPa, except for the successively loaded samples GS04 and GS11. Their final loadings reach a peak strength of 100–110 MPa (Figure 4g). All peak strengths are significantly lower than the applied peak stresses (400–500 MPa for single loadings and ~185 MPa for successive loadings). The first strain rate peak during loading, observed in all other classes, is present in this class as well. However, the most characteristic feature of these pulverized samples is the presence of a second strain rate peak after the peak strength has been reached. After its first peak, the strain rate is constant or decreases before it rises sharply toward the second strain rate peak (between 160 and 385 s^{-1}). The negative strain rate peak observed in the other classes is not observed here. The stress at the sample-input bar interface sometimes indicates a slight tensile overshoot (−25 and −35 MPa, green arrows in Figures 4g and 4h). This overshoot is caused by the duration of the applied incident stress pulse that is greater than the duration of the stress acting on the sample interfaces (dashed green line in Figure 4h). This indicates that stress is no longer transmitted across the input bar-sample interface, implying a total loss of strength and cohesion of the rock.

3.3. Damage Proxies

3.3.1. *P* and *S* Wave Velocity Measurements

P wave velocities for undamaged samples (at zero loading) fall in the range of 5350–5700 m/s, measured by the two different methods. In most cases, *P* wave velocities for class (I) samples remain constant with increasing number of successive loadings (Figure 5c), indicating that no microscopic fractures formed. With the emergence of macroscopic damage, the radial *P* wave velocities decrease to a minimum of 4000 m/s (e.g., samples G09 and G11) and axial velocities decrease at most by 500 m/s to ~5000 m/s (~90% of initial velocity).

The *P* wave velocities measured after class (II) loadings show a systematic decrease with an increase in dissipated energy (Figure 5a) or number of successive loadings (Figure 5b). The degree of absolute decrease is a function of the stress that was applied. From the intact state to failure (in this case after four loadings), the axial velocity drops by ~27% to 4000 m/s for the low-stress measurements. For the 0.5 MPa stress measurements, the absolute velocity drop measured on the same samples is much lower at ~400 m/s, possibly due to more crack closure.

Radial *P* wave velocities decrease more dramatically than axial velocities (Figures 5a and 5b): after only two loadings, a drop of ~30% is observed for class (II) samples. Since hardly any damage is visible on these samples, this means that a large amount of damage had already accumulated in an early stage of loading. The received signal for radial measurements performed on samples with higher amounts of dissipated energy (e.g., sample GS02) contained only noise, implying a very weak to nonexistent *P* wave arrival and a continuing decrease in radial *P* wave velocity.

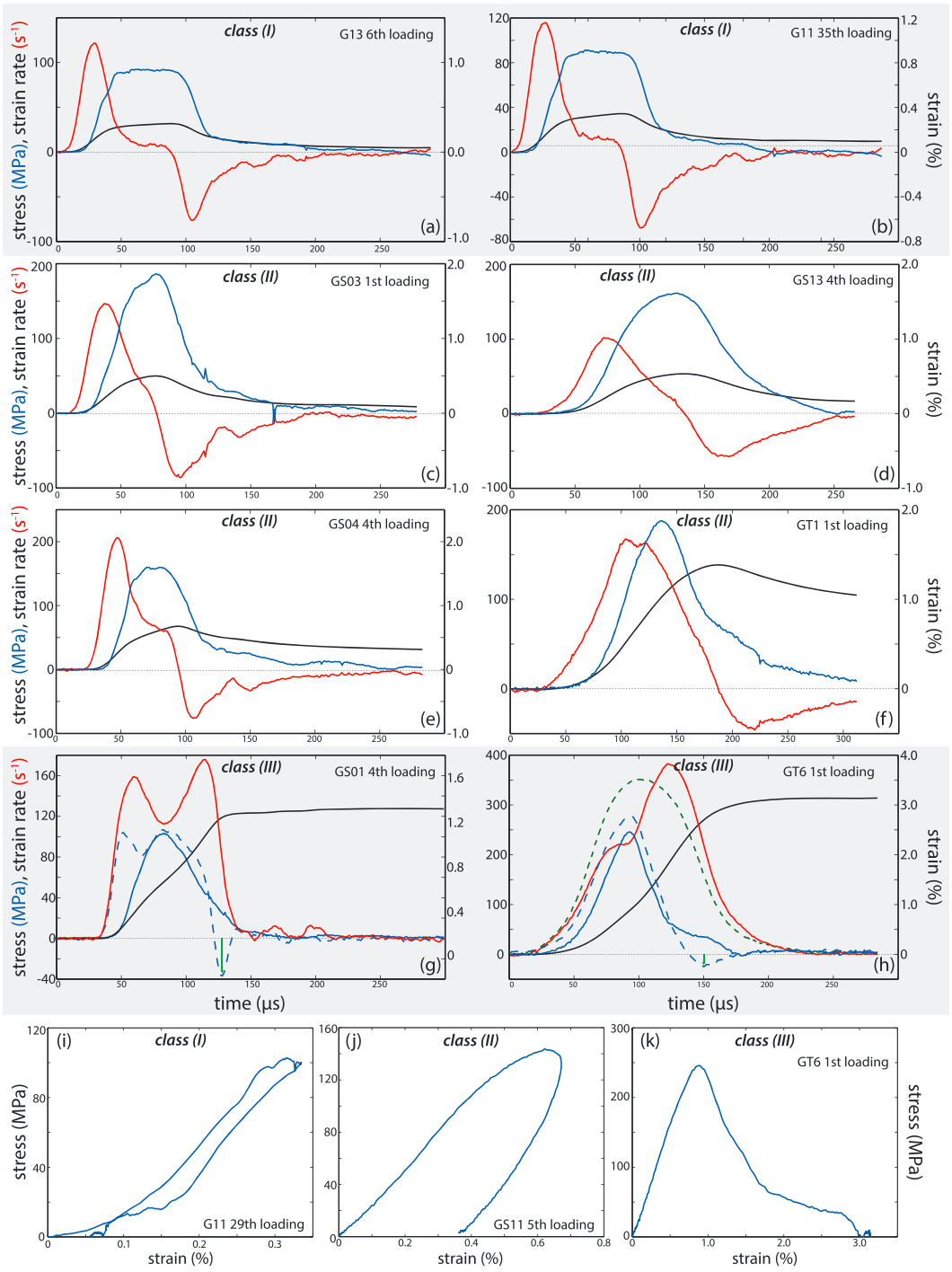

Figure 4. Stress, strain, and strain rate (blue, black, and red curves, respectively) versus time (in μs) for loadings that are typical of mechanical classes (I) to (III). (a, b) The sixth loading of sample G13 and the 35th loading of sample G11, showing elastic loading and unloading representative for class (I). Class (II) loadings include (c) the first loading of sample GS03 and (d) the fourth loading of sample GS13. Note that the strain rate "hick-up" or plateau between loading and unloading peaks has a higher strain rate relative to class (I). (e) The fourth loading of GS04 (class (II)), resulting in a fragmented sample. (f) A class (II) loading of sample GT1, resulting in a fragmented to pulverized macroscopic end state. (g, h) Two mechanical data sets representing class (III). Note that stress equilibrium conditions were not optimal for Figure 4g. These samples experience the highest strain rate after the peak stress has been reached. The green arrows indicate the tensile overshoot during unloading at the sample-input bar interface. The incident pulse (dashed green line in Figure 4h, vertically not to the same scale) shows that loading is still continuing while the strength of the sample has dropped to zero. (i–k) Stress-strain curves for class (I), class (II), and class (III) mechanical loadings, respectively.

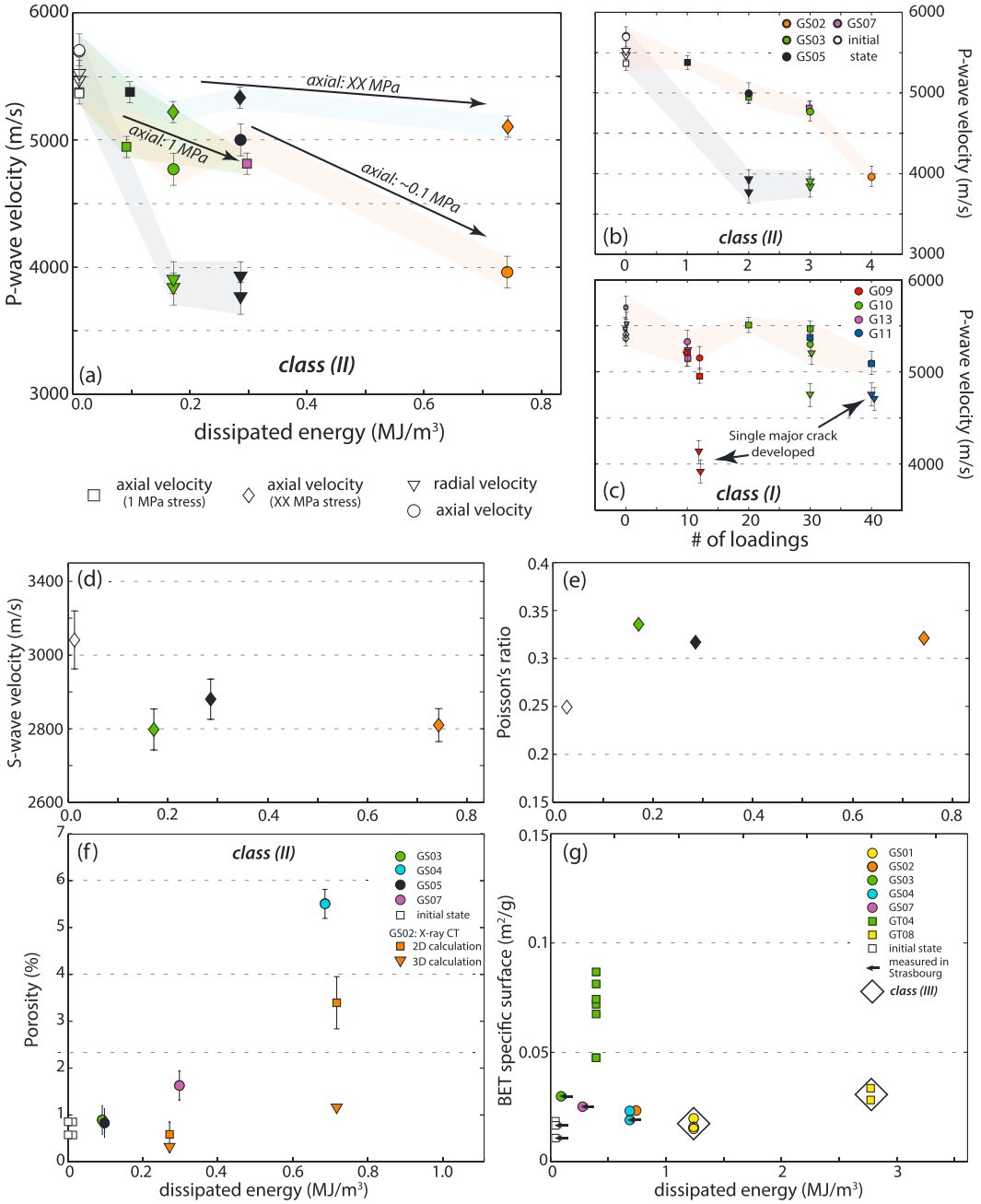

Figure 5. *P* wave velocities measured on samples with class (II) mechanical behavior (a) versus the amount of dissipated energy and (b) versus the number of loadings. (c) *P* wave velocities measured on class (I) mechanical behavior samples. For Figures 5a–5c, velocities are measured under 1 MPa stress (squares, axial direction), under 0.5 MPa (diamonds, axial direction), and without stress (circles/triangles for axial/radial direction). Note that some samples were measured multiple times after a different number of successive loadings (e.g., GS05 after one and two loadings). (d) *S* wave velocity versus dissipated energy measured in the axial direction under 0.5 MPa stress. (e) Poisson's ratio in the axial direction versus dissipated energy. The ratio is based on the *P* and *S* wave velocities measured under 0.5 MPa stress. (f) Porosity versus dissipated energy for several mechanical class (II) samples. Porosity values for sample GS02 obtained from the X-ray micro-CT data set by 2-D calculations (squares) and 3-D reconstruction (triangles) is given as well. (g) Specific surface results obtained through BET measurements versus the dissipated energy. Unless indicated, samples show class (II) mechanical behavior.

A measure of damage anisotropy is obtained when comparing the two radial and axial *P* wave velocity measurements. For class (I) samples (Figure 5c), anisotropy is observed only when a single fracture develops. For class (II) samples (Figure 5a and 5b), an axial-radial anisotropy is observed but radially there is no anisotropy. The axial-radial anisotropy increases with an increasing amount of damage.

S wave measurements were obtained only in the axial direction (Figure 5d) and decrease with increasing dissipated energy, from an initial velocity of 3100 m/s to 2600 m/s. This is significantly more than the *P* wave velocity drop measured under similar stress (Figure 5a). The change in dynamic Poisson's ratio is obtained from the *P* and *S* wave data set measured under 0.5 MPa stress (Figure 5e). The initial value of 0.25 obtained from the seismic velocities is close to the quasi-static Poisson's ratio of 0.27 obtained during the UCS test. With an increasing amount of dissipated energy, Poisson's ratio shows a maximum increase of ~0.09 to 0.34 (sample GS02, Figure 5e).

3.3.2. Porosity

Similar to the change in *P* wave velocity, the porosity for class (I) loadings (Table 2) does not change significantly with an increasing number of loadings. If anything, it seems to decrease slightly from an initial value of 0.6–0.9% to 0.47% (after 20 loadings) and 0.35% (after 30 loadings). However, error bars are ±0.3%. For class (II) loadings, the porosity hardly increases above initial values at low dissipated energy (Table 2 and Figure 5f). The porosity increases considerably to at least 5.5% with a higher dissipated energy. Thus, in contrast to the radial *P* wave velocities, the porosity increases only after much internal damage has already been introduced. Porosity values obtained by X-ray microtomography (sample GS02, see section 3.3.4) are systematically lower.

3.3.3. BET Specific Surface Area

Overall, the specific surface area values obtained by BET analysis on damaged samples are very low (of the order of 0.01–0.08 m^2/g, Figure 5g). The results from the two different BET apparatus do not show any significant difference from each other. Furthermore, the reproducibility is of the same order of magnitude as the specific surface area values, for example, the values of sample GT04 vary in the range 0.45–0.8 m^2/g. Therefore, by definition, the possible trend between specific surface area and number of loadings or (cumulative) dissipated energy (Figure 5g), if any, falls within the error bars of the measurements.

3.3.4. X-ray Microtomography

The X-ray microtomography acquisition on sample GS02 after the third loading (Figure 6a, first row) and after the fourth loading (Figure 6a, second row) shows the growth of a well-developed fracture network. Both loadings exhibit class (II) mechanical behavior. The scan taken after the third loading reveals one major fracture in 3-D reconstruction that has been developed fully along the length of the sample and parallel to the loading direction (Figure 6a, second and third columns). A low number of smaller fractures were too small for the 3-D reconstruction but are visible in the tomography data (Figure 6a, fourth column).

Surprisingly, an additional loading did not result in failure along the main fracture but led to the growth of other fractures parallel to the loading direction distributed homogenously in the sample volume (Figure 6a, second row). In the center of the sample, these new fractures show a roughly circular pattern. Toward the edge of the sample, the orientation of the fractures changes to a radial pattern, roughly perpendicular to the samples' outer surface. There is a high degree of connectivity in the macroscopic fracture network, despite the whole sample keeping some level of cohesion. The smaller fractures that were visible after three loadings (marked blue, fourth column of Figure 6a) now fall within the resolution of the 3-D reconstruction, although they have not become the most dominant. Again, some smaller fractures fall below the 3-D reconstruction resolution but are visible in the cross sections (Figure 6a, fourth column).

On a smaller scale, many fractures show a stepwise pattern in which the step tread width is greater than the riser height (Figure 6b). Although these structures suggest the formation of mode II microfractures with mode I wing cracks, they are most likely related to the cleavage planes of feldspar minerals. The local stress field can explain the opening of the step tread (Figure 6b) during loading, where σ_2 is perpendicular to the sample surface due to dynamic confinement (see supporting information S1). Most fractures avoid the highest-density minerals (pyroxenes) by changing their trajectory during propagation.

The porosity value determined from the volume of the 3-D reconstruction is less than the initial porosity of the rock (Figure 5f). The porosity values determined by 2-D analysis match the direct measurements slightly better (Figure 5f) because more fractures are included in the 2-D analysis compared to the 3-D analysis (Figure 6c, the cross section is similar to the second row of Figure 6a). Also, noise-like traces reflect where fractures smaller than the resolution limit might be (Figure 6c, green arrows), augmenting the porosity value. On the other hand, some

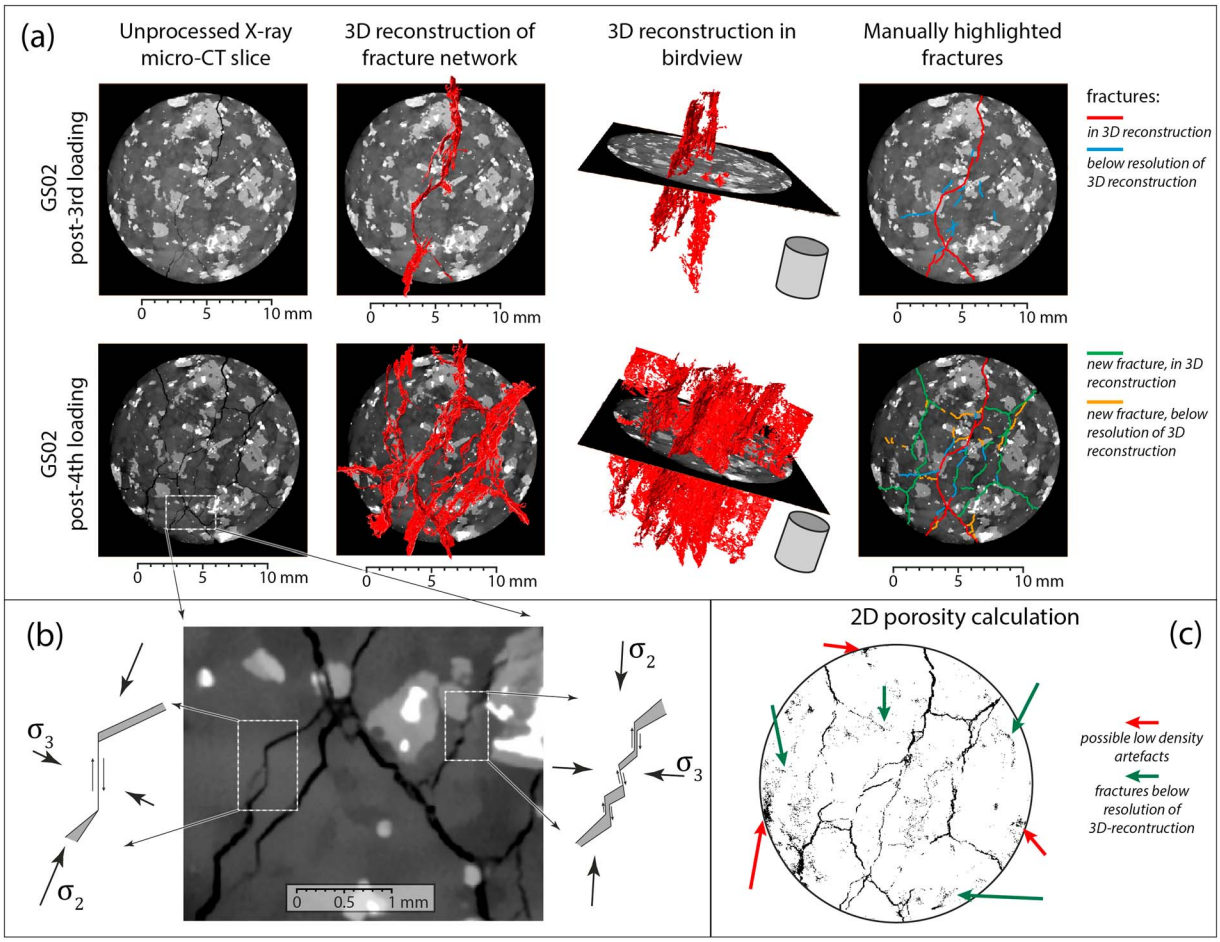

Figure 6. (a) X-ray microtomography images of sample GS02 after the third (top row) and fourth (bottom row) successive class (II) loading. The slice shown in both data sets (first column: pristine image) is taken at the same height near the middle of the sample. The second column shows a top view of the 3-D reconstruction of the fracture network; an oblique view is provided in the third column. Manually annotated fractures in the slice (fourth column) are color coded to indicate which fractures fall below and within the resolution of the 3-D reconstruction. (b) Close-up of the post–fourth loading slice in which step-shaped fractures are visible, related to feldspar cleavage planes. On the left and right sides are the interpretative sketches given of the stress state that cause dilation. (c) The post–fourth loading slice after setting a threshold for the 2-D analysis. Fractures smaller than the 3-D reconstruction resolution but included in the 2-D analysis are annotated by green arrows; low-density artifacts and regions are indicated by the red arrows.

low-density artifacts and regions are included in the calculation (Figure 6c, red arrows). The remaining difference with the measured porosity is due to a large number of fractures with apertures below the resolution of 24 μm that are connected with the main fracture network.

3.3.5. Microstructural Observations

Samples GT09 and GT10, from which thin sections were taken, experienced the same loading conditions and fall within class (III) despite the extra confinement (2.3 MPa) provided by the jacket (Figure 7a). In contrast with the unjacketed samples (Figures 4g and 4h), there is some elastic unloading visible in the strain and strain rate history and the samples do not lose their entire load-bearing capacity (Figure 7a). This is due to the jacket that prevents the fragments from flying off after the fracturing stage.

Both parallel and perpendicular to the loading direction, a large amount of fracture damage is visible (Figures 7b and 7c). All macrofractures run parallel to the loading direction (Figure 7b), similar to unconfined class (II) samples (e.g., Figure 6). A main fracture network can be recognized with broad zones of fragmented grains, which run through different minerals, except for biotite that shows clear kinking in the loading-parallel thin section (Figure 7d). Often, the major fracture zones terminate near such kinked biotites (Figure 7d, red arrow). Most fractured zones show only dilation, but some zones show a degree of offset (Figure 7b). The stepwise patterns recognized in the X-ray microtomography data (Figure 6b) are related to cleavage planes of feldspar (Figure 7c). Besides the main connected fracture network, many smaller isolated

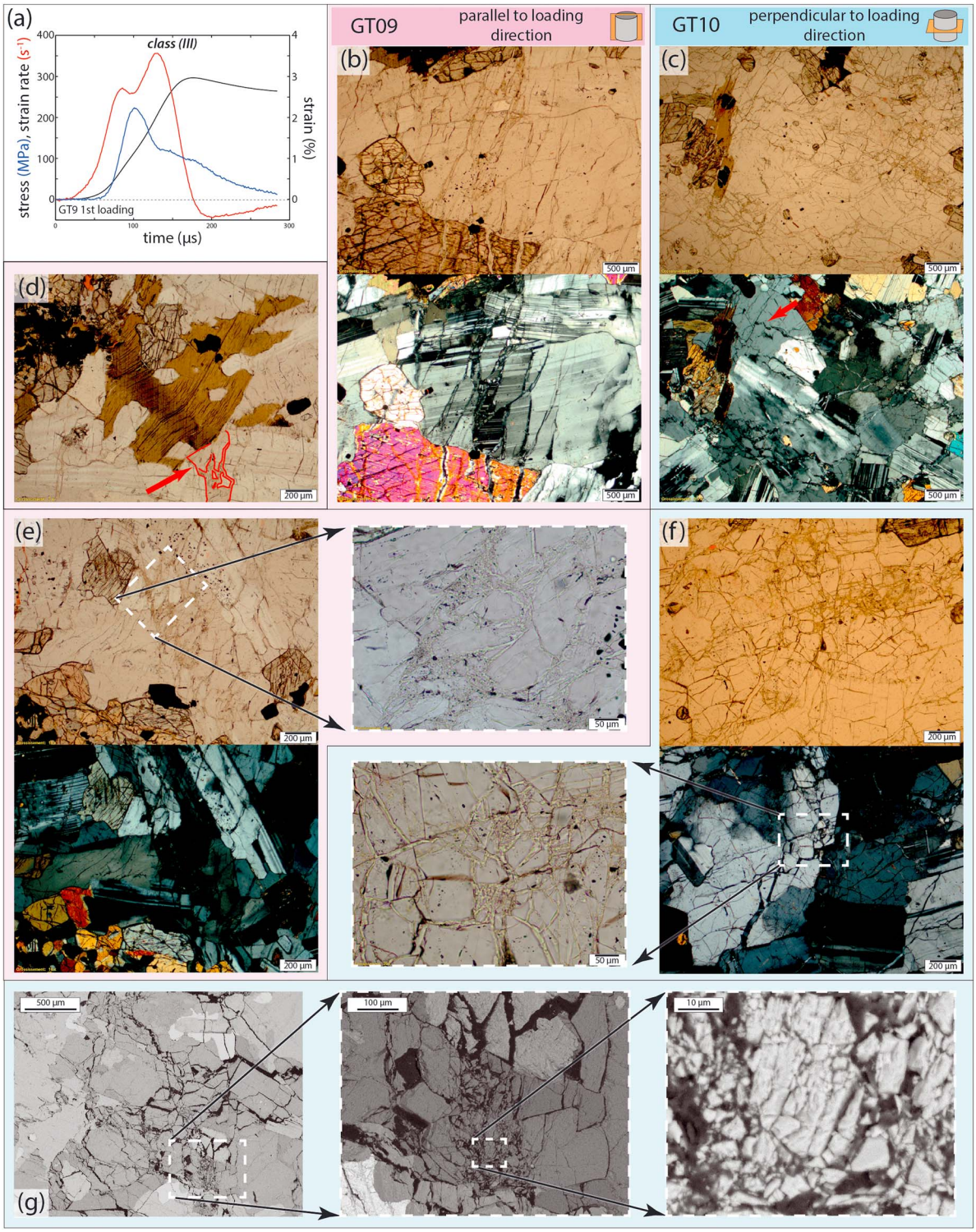

Figure 7. (a) Stress, strain, and strain rate history of jacketed sample GT09. Note the second strain rate peak and some elastic unloading. (b–f) Microphotographs of class (III) pulverized samples GT09 (pink background, parallel to loading direction) and GT10 (blue background, perpendicular to loading direction). (b) Parallel (top) and cross-polarized (bottom) images of a fracture zone running through feldspar and pyroxene. Offset by the fractures is visible in the feldspar twinning. (c) Overview of several main fracture zones forming a network with intragranular fractures in the zones in between. The red arrow indicates a wing crack geometry such as observed in the X-ray microtomography data. (d) Kinked biotite; the principal loading direction is roughly up-down. The red arrow indicates a major fracture zone (delineated by red lines) terminating near the kinked zone. This major fracture zones seems to be lacking a lot of smaller fragments. (e, f) Overview images and close-ups of finely comminuted zones with grain sizes below 10 μm. The cross-polarized light images show an in situ "explosion" without rotation of the grains. (g) SEM images that zoom in from left to right on a highly pulverized region with particles that are smaller than 1 μm.

intracrystalline fractures are recognized running parallel to the principal loading direction or following the cleavage planes of a mineral.

On a smaller scale, comminution resulted in fragments smaller than 10 μm in the major fracture zones (Figures 7e–7g). Even submicronic particles were observed with the SEM (Figure 7g), mainly concentrated in locally highly pulverized zones. Despite the large reduction in particle size, the original grain boundaries are easily recognizable and little rotation of the fragments is observed in cross-polarized light (Figures 7e and 7f). It is possible that during the processing and consolidation of the samples (i.e., sample cutting and polishing), some of these finely pulverized zones have disappeared, thus leaving large open mode fractures in the sample (e.g., the highlighted zone in Figure 7d).

4. Discussion

4.1. Criteria for Pulverization and Dynamic Fracturing

Based on previous described results, the three mechanical classes can be interpreted as follows: class (I) samples are subject to mainly elastic deformation, which causes the initial strain rate peak, and some incidental deformation expressed as a single fracture. Class (II) samples are subject to pervasive dynamic fracturing, where some samples have been sufficiently damaged to fail on the sample scale. Class (III) samples are subject to pervasive dynamic fracturing as well but lose all cohesion during catastrophic failure and become pulverized. This dynamic pulverization in experiments is characterized by the two following mechanical properties:

1. The strain rate increases, instead of decreases as in dynamic fracturing only, after the elastic loading strain rate peak is reached.
2. During this second strain rate increase, the sample loses virtually all strength.

The occurrence of this second strain rate peak is used as a criterion to determine if a sample was pulverized. This criterion is less subjective than the one based on the macroscopic description of damage used in previous studies [*Doan and Gary*, 2009; *Yuan et al*., 2011; *Doan and d'Hour*, 2012], but it does assume that pervasive dynamic fracturing and pulverization occur at or after the constant strain rate plateau or "hick-up" that acts as a hinge point in the mechanical history (Figures 4b–4h). This assumption is justified below (and in more detail in supporting information S3) by looking at theoretical considerations [from *Ashby and Sammis*, 1990; *Bhat et al*., 2012] and applying them to the experimental data. The strain rate of this hinge point can be used to define the strain rate pulverization threshold. This is in contrast with previous studies, where strain rates have been obtained by taking the maximum strain rate, excluding the pulverization-related strain rate peak [*Doan and Gary*, 2009; *Doan and Billi*, 2011; *Doan and d'Hour*, 2012], the average strain rate [*Yuan et al*., 2011], or the value of the constant strain rate plateau [*Xia et al*., 2008] without solid arguments.

From the theoretical analysis (see supporting information S3), it is argued that an increase in loading rate causes an increase in fracture initiation toughness, which then results in a higher amount of stored elastic energy before fractures are initiated (Figure 8a). It follows that more fractures in the rock can be activated with more stored elastic energy available. This thus reflects dynamic pervasive fracturing. By using the functional formulations for this process from [*Bhat et al*., 2012] on the data in the present study, the moment at which the fractures are activated is shown to agree with the hinge point in the strain rate history of the experiments (supporting information S3, Figure 8b). If enough elastic energy is available, the sample can lose all cohesion, resulting in pulverization with the typical second strain rate peak in the experiments (Figure 8b). If insufficient energy is available at the moment of initiation or during the fracture tip acceleration, pervasive fracturing is arrested (as in the early successive loadings) and pulverization does not occur (Figure 8b).

4.2. Pulverization Thresholds and the Effect of Successive Loadings

Here the pulverization thresholds for strain and strain rate are defined for single loadings [similar to *Doan and Gary*, 2009; *Doan and Billi*, 2011; *Yuan et al*., 2011; *Doan and d'Hour*, 2012]. These thresholds are then monitored to see how they change during successive loadings, and an attempt is made to generalize these results.

Samples that accumulated a total strain of more than 1.2% are pulverized. This is not influenced by single or successive loadings (Figure 9). The strain pulverization threshold is based on postloading values, reflecting the final state of the rock and not the dynamic fracturing process itself. It can therefore be interpreted as the expression of a critical damage level at which the sample has lost its cohesion (Figures 4g and 4h). This

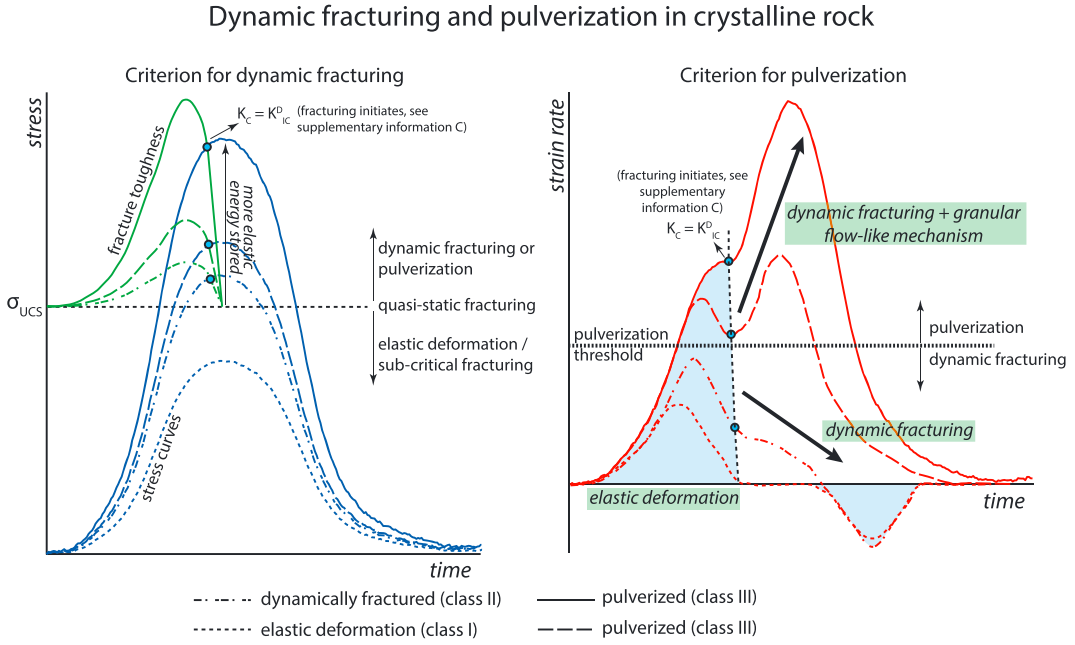

Figure 8. General behavior for dynamic stress loadings on crystalline rock. (left) The stress history (blue curves) relative to the uniaxial compressive strength (UCS) for differently deformed samples (elastic, dynamically fractured and pulverized). Sample strength is allowed to rise above the UCS due to the increase in dynamic fracture toughness (see supporting information S3). The higher the stress is allowed to rise, the more elastic energy is stored and available for fracturing at the moment that the criterion is satisfied (indicated by the blue circles). (right) Strain rate response to the loading histories on the left. Samples deform elastically at strain rates below the pulverization threshold and before the dynamic fracturing criterion is satisfied (blue area). Once the dynamic fracturing criterion is satisfied, dynamic fracturing commences. When strain rates are higher than the strain rate threshold at this moment, the sample fails catastrophically and another deformation mechanism accommodates the strain.

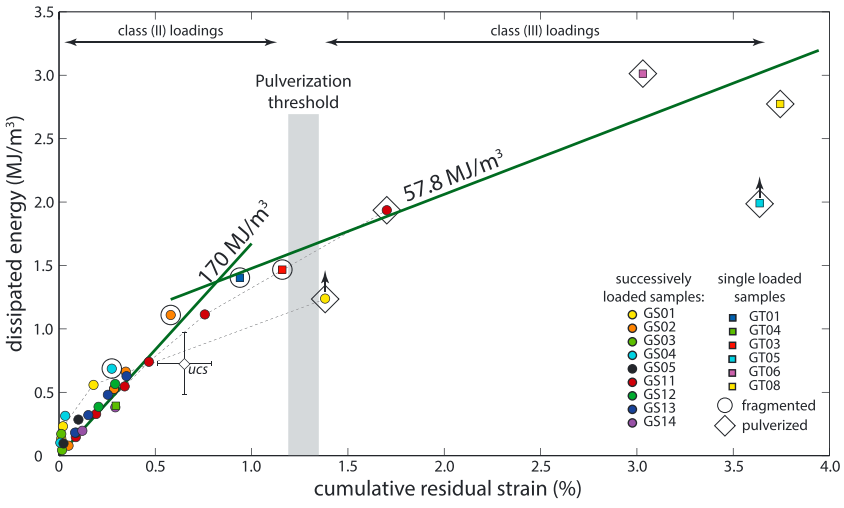

Figure 9. Cumulative residual strain versus dissipated energy for single (squares) and successive (circles) loadings, including the pulverization strain threshold (gray beam). The linear fit for the class (II) loadings (green dashed line, $R^2 = 0.86$) is forced through the origin. The linear fit for the pulverized samples (green dashed line, $R^2 = 0.90$) includes the heavily fragmented samples GT01 and GT03 and excludes samples GS01 and GT05. Black arrows indicate samples for which the calculated dissipated energy was underestimated due to stress disequilibrium issues. Note the gradual change from one energy regime to the other between ~0.65 and 1.2% strain, illustrated by the thin dashed line that connects the loadings of sample GS11. Error bars in strain and energy calculations fall below the resolution of this graph.

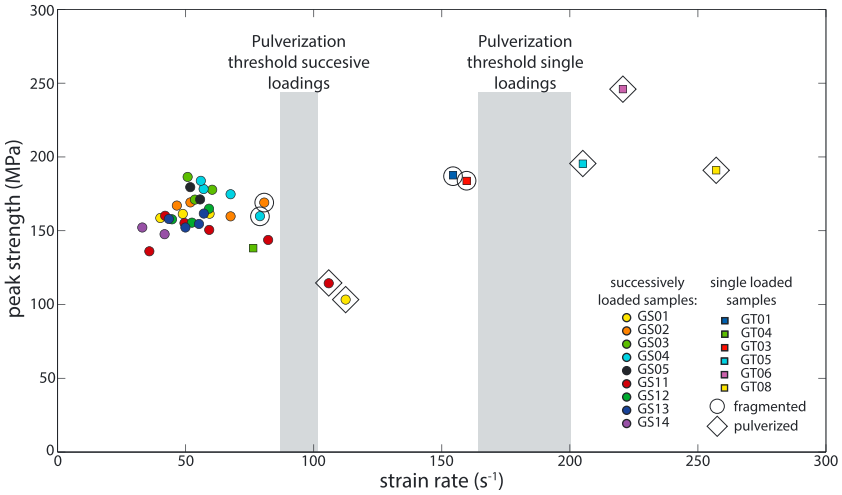

Figure 10. Strain rate at fracture initiation versus peak strength for single (squares) and successive (circles) loadings. The gray intervals indicate the pulverization thresholds for single loadings (165–200 s^{-1}) and successive loadings (85–100 s^{-1}). For successive loadings, the strain rate increases and peak strength decreases while loading conditions are similar.

is similar to the critical damage parameter suggested by *Lyakhovsky and Ben-zion* [2014] in their continuum breakage damage model. After such a transition from a damaged solid to granular (or pulverized) material, the deformation mechanism can change (Figure 8b).

The representative strain rates at the hinge point (the onset of dynamic fracturing) for single loadings reveal a strain rate threshold of 165 to 200 s^{-1} for intact rock (Figure 10). This threshold is similar to thresholds determined on similar igneous crystalline rock in the studies of *Yuan et al*. [2011] and *Doan and D'Hour* [2012]. For successive loadings, the strain rate threshold is reduced by nearly half to 85–100 s^{-1}. No significant difference in strain rate is observed between the samples pulverized after four loadings (GS04) and after six loadings (GS11). Thus, with increasing damage, the critical hinge point in strain rate for pulverization is reduced, which has been predicted by *Doan and d'Hour* [2012].

From this, it may be concluded that dynamic pervasive fracturing is the mechanism that can lead to its most extreme damage end-member: pulverization. This can be elucidated by studying the amount of dissipated energy necessary to accommodate strain (Figure 9). At low axial strains, typical for dynamically fractured samples, the energy versus strain curve is steep (170 MJ/m^3, green line in Figure 9). Note that more energy is dissipated for an equal amount of strain during dynamic loading compared to quasi-static loading (UCS tests, diamond in Figure 9). In the interval between 0.75% strain and the strain pulverization threshold, the slope changes gradually to 58 MJ/m^3. This change in slope suggests a different deformation mechanism that accommodates strain while dissipating less energy, such as granular flow and grain boundary frictional sliding when the sample is sufficiently comminuted by fracturing. A similar change in slope for the energy-strain curve has been observed for dynamically tested Carrara marble samples [*Doan and Billi*, 2011].

These findings suggest that sufficient episodes of pervasive dynamic fracturing will eventually result in pulverization of the sample once the strain threshold is exceeded. The number of successive episodes depends on the stored elastic energy that is available for each pervasive fracturing event. The stored elastic energy is reflected by the strain rate at the moment of initiation (supplementary information C). Each episode of dynamic fracturing increases the size of the flaws (fractures), thus lowering the criterion for dynamic fracturing and with it the strain rate threshold for the next event. This is well illustrated by the reduction in the UCS of dynamically damaged samples (Table 2). However, some complications should be taken into account for this relatively straightforward explanation:

1. The flaw size distribution in the rock is assumed to be narrow. This would result in a "sharp" transition from weakest-link quasi-static behavior to pervasive dynamic fracturing. Thus, at a relatively low strain rate and higher strain rate, the same amount of flaws is activated, resulting in eventual pulverization in both cases. However, with a less narrow flaw size distribution, there is a more continuous transition from localized to pervasive fracturing at relatively low strain rates. Here not all pervasive fracturing events would eventually result in pulverization, but only those at a higher strain rate would. This is well reflected in the work by *Li et al.* [2005],

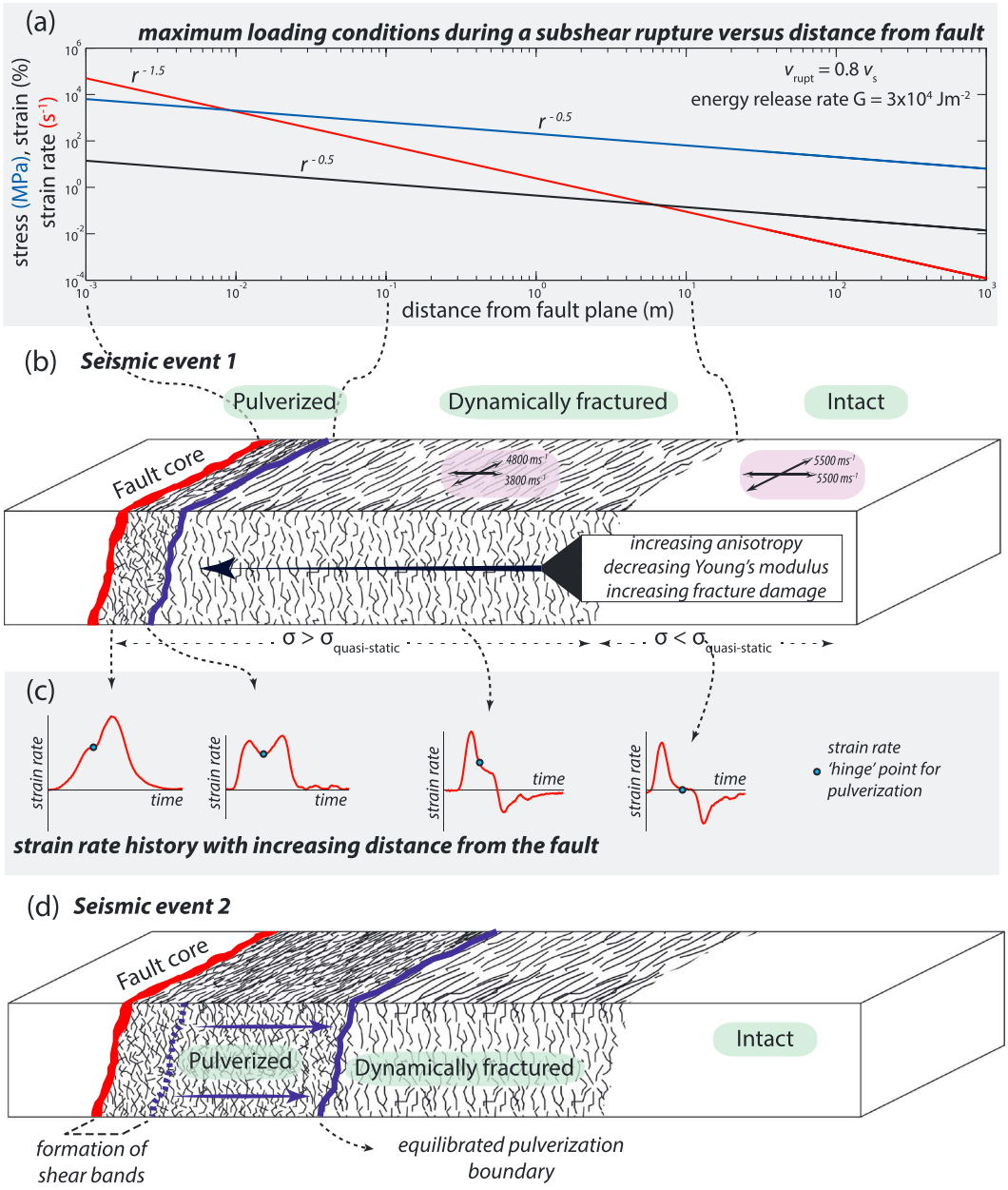

Figure 11. Schematic integration of the experimental results into a fault damage zone structure. (a) The decay of the peak loading conditions (stress, strain, and strain rate) with distance from the rupture tip or fault plane during a subshear rupture. Note that both *x* and *y* axes are logarithmic. Results are obtained using equations (4.3.23), (4.3.24), and (5.3.10), and 5.3.10 from *Freund* [1990]. Values for rupture velocity (v_{rupt}) and energy release rate are indicated. (b) Schematic damage zone structure after a first seismic event. During rupture, dynamic fracturing occurs when transient stresses reach values above the quasi-static peak strength, and pulverization occurs when the strain rate is equal to or higher than the strain rate pulverization threshold. This is illustrated for a sub-Rayleigh wave speed rupture by the dashed lines running from Figures 11a–11b. Possible variation in *P* wave velocities from an initial isotropic rock is indicated. (c) Possible strain rate histories during seismic loading for pulverization and dynamic fracturing. The blue circle indicates the crucial point of dynamic fracturing onset. (d) The damage zone after several seismic events. Dynamic damaging of the rocks reduces the pulverization threshold. Close to the fault, shear bands might form in the granular material.

on similar material where successive loadings performed at lower strain rates and stress resulted in nonpervasive fracturing and only a few fragments.

2. Related to this is the size of the volume considered. The experiments described here focus on small volumes: centimeter-scale samples. When the volume is increased, the probability of occurrence of larger-scale flaws (cm to m) becomes greater. These might act as energy sinks at high strain rates, not

allowing small-scale pulverization to occur or possibly reducing the pulverization thresholds. This effect is not addressed in this paper but will be the subject of future research.

4.3. Petrophysical Change and Microstructures

4.3.1. Dynamically Fractured Samples

Petrophysical data and microstructures help define the damage mechanism for dynamically fractured samples (class (II)). The strong decrease in *P* and *S* wave velocities at relatively low dissipated energy strongly suggests pervasive fracturing (Figure 5a). Moreover, the considerable sensitivity of *P* wave velocity to the stress applied during the measurement suggests a large amount of fracture damage. The microtomography scans provide an image of the development of a macroscopic network of fractures from one loading event to the next (Figure 6a), which indicates the generation of multiple fractures throughout the rock volume.

The nonlinear increase in porosity with dissipated energy (Figure 5f) is related to a change in the connectivity of the fracture network. The imbibition method underestimates porosity if the fracture connectivity is low. This is why samples associated with low dissipated energy show large *P* wave velocity drops and low porosities (Figures 5a and 5f). The fracture connectivity increases significantly when samples approach the pulverization threshold, resulting in a sharp increase in porosity (Figure 5f).

4.3.2. Transition to Pulverized Samples

Petrophysical properties could not be measured on pulverized samples (class (III)) due to consolidation issues. The change in petrophysical properties can however be discussed by means of microstructural observations.

The main difference between dynamically fractured (Figure 6) and pulverized (Figure 7) rocks is the zones of finely comminuted material in the main fracture network of the latter (e.g., Figure 7g). The finely comminuted fracture zones are 50–200 μm wide and filled with particles. Therefore, the bulk density of these zones would be slightly lower. In contrast, the fractures (~50–100 μm in width) in the tomography data show the lowest density values. Thus, in spite of the lower resolution of the microtomography, these finely comminuted zones would have been recognized if they were present in the dynamically fractured samples. The gradual transition observed in the dissipated energy versus strain plot (Figure 9) suggests that local pulverization already occurs before bulk pulverization is reached. This is supported by the heterogeneous distribution of the finely pulverized zones observed in the microscopic study. As discussed earlier, the change in slope reflects a change in deformation mechanism. This is well illustrated by zones of very fine-grained material (Figures 7e–7g) in which granular flow or grain boundary friction could occur. There is also some offset between fragments (Figure 7b).

The fine-grained fracture zones in pulverized rocks could inhibit fluid flow (and thus permeability) compared to highly damaged dynamically fractured rocks because the tortuosity increases. Regarding fluid storage capacity or porosity, allowance should be made for the possibility that dilation was restricted for the pulverized samples by their jackets. Even so, the change in permeability from an intact rock to a dynamically fractured and then to a pulverized rock is expected to show a nonlinear increase followed by a break in the trend at the pulverization threshold, possibly even a reduction in permeability.

4.4. Successive Loadings and Implications for Active Faults

4.4.1. Rupture Models Able to Provide High Strain Rates

The previously discussed criteria for pervasive dynamic fracturing and pulverization are applied to active fault here, based on experimental data (Figure 8) and the strain and strain rate pulverization thresholds. To this end, the loading conditions of the experiments need to be compared with the loading conditions of stress waves radiating from a passing earthquake rupture tip.

The most important loading condition is loading rate or strain rate, since it needs to be sufficiently high for dynamic pervasive fracturing to occur and to exceed the pulverization threshold. The amplitude or maximum stress of the stress waves is then important, as it needs to exceed the quasi-static peak stress in order to allow dynamic pervasive fracturing to occur. The total strain caused by each loading is less important because the pulverization strain threshold is fixed (Figure 9).

Several rupture models predict sufficiently high stress or strain rate loadings.

1. Sub-Rayleigh wave speed rupture models have a transient stress field that can be predicted by linear elastic fracture mechanics. The model predicts an asymptotic stress field that decays by $1/r^{0.5}$ for the stress and strain and by $1/r^{1.5}$ for the strain rate, with r being the distance to the rupture tip [*Freund*, 1990] (Figure 11a). These formulations have been experimentally verified by *Svetlizky and Fineberg* [2014]. Such a rupture would thus

result in dynamic fracturing at small distances from the fault [*Doan and Gary*, 2009; *Doan and Billi*, 2011], possibly contributing to comminuted and sheared fault rocks such as gouge and cataclasites [*Reches and Dewers*, 2005]. However, evidence for dynamic fracturing in the form of pulverized rocks is found hundreds of meters from the fault [*Brune*, 2001; *Dor et al*., 2006b; *Mitchell et al*., 2011] and cannot be explained by sub-Rayleigh wave speed ruptures [*Doan and Gary*, 2009].

2. Supershear velocity rupture models predict high strain rates at a substantial distance from the fault plane because the *S* wave contribution is a Mach cone that does not decay with distance up to a length scale that is related to the maximum depth of the seismogenic zone [*Dunham and Bhat*, 2008; *Ampuero*, 2014]. It should be noted, however, that this involves *S* wave loading, a loading configuration that is not possible in the experimental setup described here.
3. Ruptures along bimaterial interfaces also provide high strain rates at greater distances from the fault [*Ben-Zion and Shi*, 2005; *Shi and Ben-zion*, 2006; *Ampuero and Ben-Zion*, 2008]. These so-called Weertman or wrinkle-like pulses cause tensile loading perpendicular to the fault on the stiffer side of the fault [*Weertman*, 1980; *Adams*, 1995; *Andrews and Ben-Zion*, 1997]. Such a model could explain the observed asymmetric distribution of pulverized rock observed in the field [*Dor et al*., 2006a, 2009; *Mitchell et al*., 2011]. However, loading in tension might not be similar to loading in compression as in these experiments.
4. Another rupture model that can accommodate off-fault high-strain rate loading at lengthy distances involves asperities or barriers causing a local acceleration or deceleration of the rupture tip. This leads to local transitions to and from supershear speeds [*Dunham et al*., 2003] and circumvents the problem of rarely observed stable supershear earthquakes. It might also explain the patchy distribution of pulverized rocks [*Dor et al*., 2006a].

4.4.2. Fault Damage Zone Structure by Successive Loadings

Regardless of which of the above models is applied to a fault, the effect of successive loadings on the damage zone architecture is similar and only the length scale perpendicular to the fault changes. Damage zones of mature fault systems (displacement $>$ 100 m) rarely exceed widths of the order of 100 m [*Faulkner et al*., 2011; *Savage and Brodsky*, 2011]. This boundary might coincide with the point at which the strain rate field radiating from the rupture tip is too small and stresses drop below the quasi-static peak strength of the rock (Figures 11a and 11b). Some brittle creep-like behavior might occur beyond this point, but the contribution to the damage zone is negligible. The strain rate response is purely elastic (Figure 11c).

Closer to the fault core, the rocks experience peak stresses above the quasi-static peak stress. Here the strain rates are below the pulverization threshold for intact rock but high enough for pervasive dynamic fracturing (Figure 11c). For this zone, the elastic moduli that have been determined from experiments show that Young's modulus decreases by at least 50% for the stiffest direction (perpendicular to the loading direction) and Poisson's ratio increases from 0.25 to 0.34. The coseismic change in the elastic moduli on the scale of the damage zone might influence rupture propagation and slip distribution [e.g., *Cappa et al*., 2014]. It also makes the damage zone more compliant for future ruptures and aftershocks.

Even closer to the fault core, the strain rate conditions at the onset of fracture pass the pulverization strain rate threshold for intact rock (Figure 11c). A band of pulverized rock forms (Figure 11b). Some shear strain can be accommodated after catastrophic failure as the rock has changed into a granular material. At very small distances from the rupture (mm scale), loading conditions might be high enough to cause gouge-like pulverization, as suggested by *Reches and Dewers* [2005]. However, at such high loading rates, comminution might be accommodated by mechanisms other than breakage [*Grady*, 1998].

The following seismic events do not shift the outer boundary of the damage zone outward, unless the event produces higher loading conditions (stress and loading rate) due to a higher magnitude or if the rock is weakened by non-coseismic deformation. The pulverization boundary migrates outward due to the drop in pulverization strain rate threshold and in quasi-static peak stress (Figure 11d). More damage is accumulated in the dynamically fractured rocks that have not been pulverized, potentially bringing them below the pulverization thresholds for future seismic event. In addition, the elastic moduli of the damage zone rocks progressively drop. The already pulverized rocks close to the fault core can accumulate shear strain and turn into cataclasites.

This experimentally based conceptual fault zone structure of intact-fractured-pulverized-sheared fault rocks is similar to field observations [*Dor et al*., 2006b; *Mitchell et al*., 2011; *Rempe et al*., 2013]. Moreover, *P* wave velocities measured in the field decrease with decreasing distance from the fault within the fractured rock zone [*Rempe et al*., 2013]. This drop in *P* wave velocity measured on their oriented hand samples shows a

comparable anisotropy to the laboratory samples described in this study. The relationship between rupture models and damage anisotropy is briefly discussed below.

4.4.3. Damage Anisotropy and Rupture Models

These experiments show that anisotropy is related to the direction of loading, and the damage anisotropy observed in the field could thus shed light on past transient loading conditions. However, the upscaling from a 1-D setup in the laboratory, where the direction of loading is well defined, to a real-life 3-D triaxial situation is not straightforward. The direction of maximum principal stress, strain, and strain rate does not have to be the same and may change when an earthquake rupture tip passes by. The maximum principal stress direction is not considered here since allowance must be made for the far-field stress direction, which varies for each setting. Therefore, the maximum strain rate direction is the only parameter to be considered because the far-field strain rate is negligible with respect to coseismic strain rates.

For a given point close to a fault, the maximum strain rate direction rotates when an earthquake rupture tip passes with a sub-Rayleigh wave speed. This direction changes from nearly fault parallel to fault perpendicular and even to higher angles once the rupture tip has passed by. The maximum strain rate direction rotates during the highest stress loading (illustrated by the particle velocity field and its gradient in *Mello et al*. [2010]). Therefore, a strong damage anisotropy is not expected.

In contrast, the *S* wave Mach cone of a supershear rupture shows a more unidirectional maximum strain rate direction [*Mello et al*., 2010]. The angle of the maximum strain rate direction with respect to the fault changes with rupture velocity. Nonetheless, a more well-defined damage anisotropy might be expected. *Bhat et al*. [2007] propose that such supershear loading was the cause of fault-parallel fracturing during the 2001 Kokoxili (Kunlun) earthquake in Tibet.

Tensile loading perpendicular to the fault plane caused by wrinkle-like rupture pulses [*Weertman*, 1980; *Adams*, 1995; *Andrews and Ben-Zion*, 1997] would also result in a damage anisotropy. This rupture mechanism has been proposed to explain the observed damage anisotropy in the near-fault pulverized rock measured by *Rempe et al*. [2013].

It is unknown if pulverized rocks formed at depth contain damage anisotropy as well. Dynamic loading experiments with confining pressure could answer this question.

4.4.4. Healing, the Earthquake Energy Budget, and Other Considerations

An important factor that should not be neglected is the healing of fracture damage during interseismic periods [*Brantley et al*., 1990; *Gratier et al*., 2013b]. Without such a healing, the entire damage zone would progressively broaden with time. Moreover, healing and damage might reach an equilibrium state in which case the pulverization boundary would stagnate. For mature faults such as the San Andreas fault and Arima-Takatsuki Tectonic Line [*Mitchell et al*., 2011; *Rempe et al*., 2013], such a boundary would be located at 50 m and ~200 m from the fault core for pulverized and dynamically fractured zones, respectively.

The fraction of the earthquake energy budget that is dissipated into fracture energy cannot be determined directly from these experiments given that only one seismic wave is considered and no allowance is made for far-field stresses. However, the dissipated energy values determined from the experiments (Figure 9) show that rocks below the pulverization threshold dissipate more energy than quasi-static fractured rocks. The considerable reduction in grain size in some zones of the sample (Figure 7g) illustrates this. Above the threshold, the rock dissipates less energy due to the change in deformation mechanism. Real-life mature faults establish a stationary pulverization boundary and, as a result, not much energy can be dissipated into newly pulverized rocks. However, extreme rupture events (e.g., supershear ruptures) might dissipate relatively more energy in fractures because they can cause dynamic fracturing and pulverization at distances further than the stationary pulverization boundary.

Other factors to be considered for coseismic damage generation are depth and fluids. The experiments described here were performed without confining pressure and are therefore only representative of subsurface conditions. With increasing depth, the pulverization strain rate threshold increases, as observed by *Yuan et al*. [2011] for single-loading experiments. Therefore, it is to be expected that the zone of pulverized rock will decrease in width. The zone of dynamically fractured rock will also become smaller. Another important factor is the influence of fluids on the dynamic mechanical behavior during stress wave loading. Although, to the authors' knowledge, dynamic uniaxial compressive loading experiments on fluid-saturated crystalline rocks have never been performed, high-velocity friction experiments suggest a faster accumulation of damage in

the early loading stages [*Violay et al.*, 2013]. In the event of a fast loading rate, a rock sample would behave as an undrained rock, introducing poroelastic effects and possibly reducing the pulverization threshold. This might explain dynamic damage at greater depths.

5. Conclusions

This study shows that apparently intact and fragmented samples below the pulverization threshold experience dynamic pervasive fracturing. Dynamic fracturing and dynamic pulverization have distinctively different mechanical loading histories and, based on these differences, criteria are proposed to distinguish pulverization from dynamic fracturing in experiments. It has been shown that pulverized samples experience intense dynamic fracturing followed by a transition to a more easily deformable noncohesive granular material at 1.2% strain. To achieve enough dynamic fracture damage, the strain rate at the onset of fracturing needed to be 165–200 s^{-1} for an initially undamaged quartz-monzonite. The successive loading experiments show that, over the course of four to six loadings, damage increases and elastic moduli decrease before the sample is pulverized. The strain rate pulverization threshold was reduced by 50% after successive loadings to 85–100 s^{-1}. The prerequisite for a reduction in the pulverization threshold is that dynamic fracturing must occur in the preceding successive loadings.

The mechanical results and damage proxies are presented in the form of a conceptual damage zone model that takes field observations into account. The damage zone contains a band of pulverized rocks that broadens progressively with each seismic event by overprinting the dynamically fractured rocks. The outer boundary of the zone of dynamically fractured rocks remains stationary with successive seismic events, unless the events increase in magnitude. Furthermore, the mechanical criteria for pulverization and dynamic fracturing as well as the *P* and *S* wave velocities obtained from dynamically fractured samples provide useful insights for modeling damage zone evolution and seismic ruptures.

Acknowledgments

This project has received funding from the European Union's Seventh Framework Programme for Research, Technological Development and Demonstration under grant agreement no. 316889 (ITN FlowTrans). Funding from Labex OSUG@2020 (Investissement d'avenir-ANR10-LABX56) is acknowledged. The authors would also like to thank Joséphine Gervin for the data acquisition system on the SHPB, Valerie Magnin for the BET measurements at ISTerre, P. Charrier for his assistance with the X-ray microtomography at 3S-R, A. Steyer for technical support with equipment development in Strasbourg, and Steve Boon at UCL. T.M.M. acknowledges support from NERC grant ref NE/M004716/1. All data used are listed in the figures, tables and supporting information.

Reference

Adams, G. G. (1995), Self-excited oscillations of two elastic half-spaces sliding with a constant coefficient of friction, *J. Appl. Mech.*, *62*(4), 867–872, doi:10.1115/1.2896013.

Ampuero, J.-P. (2014), Physical limits on damaged fault zone thickness: The role of seismogenic depth, in *AGU Fall Meeting 2014*, San Francisco.

Ampuero, J.-P., and Y. Ben-Zion (2008), Cracks, pulses and macroscopic asymmetry of dynamic rupture on a bimaterial interface with velocity-weakening friction, *Geophys. J. Int.*, *173*(2), 674–692, doi:10.1111/j.1365-246X.2008.03736.x.

Andrews, D. J. (2005), Rupture dynamics with energy loss outside the slip zone, *J. Geophys. Res.*, *110*, 1–14, doi:10.1029/2004JB003191.

Andrews, D. J., and Y. Ben-Zion (1997), Wrinkle-like slip pulse on a fault between different materials, *J. Geophys. Res.*, *102*(B1), 553–571, doi:10.1029/96JB02856.

Ashby, M. F., and C. G. Sammis (1990), The damage mechanics of brittle solids in compression, *Pure Appl. Geophys.*, *133*(3), 489–521.

Ben-Zion, Y., and J.-P. Ampuero (2009), Seismic radiation from regions sustaining material damage, *Geophys. J. Int.*, *178*(3), 1351–1356, doi:10.1111/j.1365-246X.2009.04285.x.

Ben-Zion, Y., and Z. Shi (2005), Dynamic rupture on a material interface with spontaneous generation of plastic strain in the bulk, *Earth Planet. Sci. Lett.*, *236*(1-2), 486–496, doi:10.1016/j.epsl.2005.03.025.

Bhat, H. S., R. Dmowska, G. C. P. King, Y. Klinger, and J. R. Rice (2007), Off-fault damage patterns due to supershear ruptures with application to the 2001 Mw 8.1 Kokoxili (Kunlun) Tibet earthquake, *J. Geophys. Res.*, *112*, B06301, doi:10.1029/2006JB004425.

Bhat, H. S., A. J. Rosakis, and C. G. Sammis (2012), A micromechanics based constitutive model for brittle failure at high strain rates, *J. Appl. Mech.*, *79*, 031016.1–031016.12, doi:10.1115/1.4005897.

Brantley, S. L., B. Evans, S. H. Hickman, and D. A. Crerar (1990), Healing in microcracks in quartz: Implications for fluid flow, *Geology*, *18*, 136–139.

Bruhn, R. L., W. T. Parry, W. A. Yonkee, and T. Thompson (1994), Fracturing and hydrothermal alteration in normal fault zones, *Pure Appl. Geophys.*, *142*(3), 609–644, doi:10.1007/BF00876057.

Brune, J. N. (2001), Fault-normal dynamic unloading and loading: An explanation for "non-gouge" rock powder and lack of fault-parallel shear bands along the San Andreas fault, in *AGU Fall Meeting 2001*, San Francisco.

Cappa, F., C. Perrin, I. Manighetti, and E. Delor (2014), Off-fault long-term damage: A condition to account for generic, triangular earthquake slip profiles, *Geochem. Geophys. Geosyst.*, *15*, 1476–1493, doi:10.1002/2013GC005182.

Chen, W. W., and B. Song (2010), *Split Hopkinson (Kolsky) Bar Design, Testing and Applications*, Springer, New York.

Doan, M.-L., and A. Billi (2011), High strain rate damage of Carrara marble, *Geophys. Res. Lett.*, *38*, L19302, doi:10.1029/2011GL049169.

Doan, M.-L., and V. D'Hour (2012), Effect of initial damage on rock pulverization along faults, *J. Struct. Geol.*, *45*, 113–124, doi:10.1016/j.jsg.2012.05.006.

Doan, M.-L., and G. Gary (2009), Rock pulverization at high strain rate near the San Andreas fault, *Nat. Geosci.*, *2*(10), 709–712, doi:10.1038/ngeo640.

Dor, O., T. K. Rockwell, and Y. Ben-Zion (2006a), Geological observations of damage asymmetry in the structure of the San Jacinto, San Andreas and Punchbowl Faults in Southern California: A possible indicator for preferred rupture propagation direction, *Pure Appl. Geophys.*, *163*, 301–349, doi:10.1007/s00024-005-0023-9.

Dor, O., Y. Ben-Zion, T. K. Rockwell, and J. N. Brune (2006b), Pulverized rocks in the Mojave section of the San Andreas Fault Zone, *Earth Planet. Sci. Lett.*, *245*(3-4), 642–654, doi:10.1016/j.epsl.2006.03.034.

Dor, O., J. S. Chester, Y. Ben-Zion, J. N. Brune, and T. K. Rockwell (2009), Characterization of damage in sandstones along the Mojave section of the San Andreas Fault: Implications for the shallow extent of damage generation, *Appl. Geophys.*, *166*, 1747–1773, doi:10.1007/s00024-009-0516-z.

Dunham, E. M., and H. S. Bhat (2008), Attenuation of radiated ground motion and stresses from three-dimensional supershear ruptures, *J. Geophys. Res.*, *113*, B08319, doi:10.1029/2007JB005182.
Dunham, E. M., P. Favreau, and J. M. Carlson (2003), A supershear transition mechanism for cracks, *Science*, *299*(5612), 1557–1559, doi:10.1126/science.1080650.
Faulkner, D. R., A. C. Lewis, and E. H. Rutter (2003), On the internal structure and mechanics of large strike-slip fault zones: Field observations of the Carboneras fault in southeastern Spain, *Tectonophysics*, *367*(3-4), 235–251, doi:10.1016/S0040-1951(03)00134-3.
Faulkner, D. R., T. M. Mitchell, D. Healy, and M. J. Heap (2006), Slip on "weak" faults by the rotation of regional stress in the fracture damage zone, *Nature*, *444*(7121), 922–5, doi:10.1038/nature05353.
Faulkner, D. R., T. M. Mitchell, E. Jensen, and J. Cembrano (2011), Scaling of fault damage zones with displacement and the implications for fault growth processes, *J. Geophys. Res.*, *116*, B05403, doi:10.1029/2010JB007788.
Fineberg, J., S. Gross, M. Marder, and H. Swinney (1991), Instability in dynamic fracture, *Phys. Rev. Lett.*, *67*(4), 457–460, doi:10.1103/PhysRevLett.67.457.
Freund, L. B. (1990), *Dynamic Fracture Mechanics*, Cambridge Univ. Press, Cambridge.
Gama, B. A., S. L. Lopatnikov, and J. W. Gillespie (2004), Hopkinson bar experimental technique: A critical review, *Appl. Mech. Rev.*, *57*(4), 223, doi:10.1115/1.1704626.
Grady, D. E. (1998), Shock-wave compression of brittle solids, *Mech. Mater.*, *29*(3-4), 181–203, doi:10.1016/S0167-6636(98)00015-5.
Graff, K. F. (1991), *Wave Motion in Elastic Solids*, Dover, New York.
Gratier, J.-P., F. Thouvenot, L. Jenatton, A. Tourette, M.-L. Doan, and F. Renard (2013a), Geological control of the partitioning between seismic and aseismic sliding behaviours in active faults: Evidence from the Western Alps, France, *Tectonophysics*, *600*, 226–242, doi:10.1016/j.tecto.2013.02.013.
Gratier, J.-P., D. K. Dysthe, and F. Renard (2013b), The role of pressure solution creep in the ductility of the Earth, *Adv. Geophys.*, *54*, 47–179, doi:10.1016/B978-0-12-380940-7.00002-0.
Griffith, W. A., T. M. Mitchell, J. Renner, and G. Di Toro (2012), Coseismic damage and softening of fault rocks at seismogenic depths, *Earth Planet. Sci. Lett.*, *353-354*, 219–230, doi:10.1016/j.epsl.2012.08.013.
Huang, Y., and J.-P. Ampuero (2011), Pulse-like ruptures induced by low-velocity fault zones, *J. Geophys. Res.*, *116*, B12307, doi:10.1029/2011JB008684.
Huang, Y., J.-P. Ampuero, and D. V. Helmberger (2014), Earthquake ruptures modulated by waves in damaged fault zones, *J. Geophys. Res. Solid Earth*, *119*, 3133–3154, doi:10.1002/2014JB011151.
Johri, M., E. M. Dunham, M. D. Zoback, and Z. Fang (2014), Predicting fault damage zones by modeling dynamic rupture propagation and comparison with field observations, *J. Geophys. Res. Solid Earth*, *119*, 1–22, doi:10.1002/2013JB010335.
Kolsky, H. (1949), An investigation of the mechanical properties of materials at very high rates of loading, *Proc. Phys. Soc. Sect. B*, *62*(11), 676, doi:10.1088/0370-1301/62/11/302.
Li, X. B., T. S. Lok, and J. Zhao (2005), Dynamic characteristics of granite subjected to intermediate loading rate, *Rock Mech. Rock Eng.*, *38*(1), 21–39, doi:10.1007/s00603-004-0030-7.
Lockner, D. A. (1998), A generalized law for brittle deformation of Westerly granite, *J. Geophys. Res.*, *103*(B3), 5107–5123, doi:10.1029/97JB03211.
Lockner, D. A., C. Morrow, D. Moore, and S. Hickman (2011), Low strength of deep San Andreas fault gouge from SAFOD core, *Nature*, *472*(7341), 82–85, doi:10.1038/nature09927.
Lyakhovsky, V., and Y. Ben-zion (2014), Damage-breakage rheology model and solid-granular transition near brittle instability, *J. Mech. Phys. Solids*, *64*, 184–197, doi:10.1016/j.jmps.2013.11.007.
Mello, M., H. S. Bhat, A. J. Rosakis, and H. Kanamori (2010), Identifying the unique ground motion signatures of supershear earthquakes: Theory and experiments, *Tectonophysics*, *493*(3-4), 297–326, doi:10.1016/j.tecto.2010.07.003.
Mitchell, T. M., Y. Ben-Zion, and T. Shimamoto (2011), Pulverized fault rocks and damage asymmetry along the Arima-Takatsuki Tectonic Line, Japan, *Earth Planet. Sci. Lett.*, *308*(3-4), 284–297, doi:10.1016/j.epsl.2011.04.023.
Moore, D. E., and M. J. Rymer (2012), Correlation of clayey gouge in a surface exposure of serpentinite in the San Andreas Fault with gouge from the San Andreas Fault Observatory at Depth (SAFOD), *J. Struct. Geol.*, *38*, 51–60, doi:10.1016/j.jsg.2011.11.014.
Noda, H., and N. Lapusta (2013), Stable creeping fault segments can become destructive as a result of dynamic weakening, *Nature*, *493*(7433), 518–21, doi:10.1038/nature11703.
Ravichandran, G., and G. Subhash (1994), Critical appraisal of limiting strain rates for compression testing of ceramics in a split Hopkinson pressure bar, *J. Am. Ceram. Soc.*, *77*(1), 263–267.
Reches, Z., and T. A. Dewers (2005), Gouge formation by dynamic pulverization during earthquake rupture, *Earth Planet. Sci. Lett.*, *235*(1-2), 361–374, doi:10.1016/j.epsl.2005.04.009.
Rempe, M., T. M. Mitchell, J. Renner, S. Nippress, Y. Ben-Zion, and T. K. Rockwell (2013), Damage and seismic velocity structure of pulverized rocks near the San Andreas Fault, *J. Geophys. Res. Solid Earth*, *118*, 2813–2831, doi:10.1002/jgrb.50184.
Rockwell, T. K., M. Sisk, G. Girty, O. Dor, N. Wechsler, and Y. Ben-Zion (2009), Chemical and physical characteristics of pulverized Tejon Lookout granite adjacent to the San Andreas and Garlock faults: Implications for earthquake physics, *Pure Appl. Geophys.*, *166*(10-11), 1725–1746, doi:10.1007/s00024-009-0514-1.
Rowe, C. D., and W. A. Griffith (2015), Do faults preserve a record of seismic slip: A second opinion, *J. Struct. Geol.*, *78*, doi:10.1016/j.jsg.2015.06.006.
Savage, H. M., and E. E. Brodsky (2011), Collateral damage: Evolution with displacement of fracture distribution and secondary fault strands in fault damage zones, *J. Geophys. Res.*, *116*, B03405, doi:10.1029/2010JB007665.
Scholz, C. H. (2002), *The Mechanics of Earthquakes and Faulting*, 2nd ed., Cambridge Univ. Press, Cambridge.
Sharon, E., and J. Fineberg (1999), Confirming the continuum theory of dynamic brittle fracture for fast cracks, *Nature*, *397*(6717), 333–335, doi:10.1038/16891.
Shi, Z., and Y. Ben-zion (2006), Dynamic rupture on a bimaterial interface governed by slip-weakening friction, *Geophys. J. Int.*, *165*(2), 469–484, doi:10.1111/j.1365-246X.2006.02853.x.
Svetlizky, I., and J. Fineberg (2014), Classical shear cracks drive the onset of dry frictional motion, *Nature*, *509*(7499), 205–208, doi:10.1038/nature13202.
Violay, M., S. Nielsen, E. Spagnuolo, D. Cinti, G. Di Toro, and G. Di Stefano (2013), Pore fluid in experimental calcite-bearing faults: Abrupt weakening and geochemical signature of co-seismic processes, *Earth Planet. Sci. Lett.*, *361*, 74–84, doi:10.1016/j.epsl.2012.11.021.
Wechsler, N., E. E. Allen, T. K. Rockwell, G. Girty, J. S. Chester, and Y. Ben-Zion (2011), Characterization of pulverized granitoids in a shallow core along the San Andreas Fault, Littlerock, CA, *Geophys. J. Int.*, *186*(2), 401–417, doi:10.1111/j.1365-246X.2011.05059.x.
Weertman, J. (1980), Unstable slippage across a fault that separates elastic media of different elastic constants, *J. Geophys. Res.*, *85*(B3), 1455–1461, doi:10.1029/JB085IB03p01455.
Wilson, B., T. Dewers, Z. Reches, and J. N. Brune (2005), Particle size and energetics of gouge from earthquake rupture zones, *Geophys. Res. Lett.*, *434*, 749–752, doi:10.1029/2003GL019277.

Xia, K., M. H. B. Nasseri, B. Mohanty, F. Lu, R. Chen, and S. N. Luo (2008), Effects of microstructures on dynamic compression of Barre granite, *Int. J. Rock Mech. Min. Sci.*, *45*, 879–887, doi:10.1016/j.ijrmms.2007.09.013.

Xu, S., and Y. Ben-Zion (2013), Numerical and theoretical analyses of in-plane dynamic rupture on a frictional interface and off-fault yielding patterns at different scales, *Geophys. J. Int.*, *193*(1), 304–320, doi:10.1093/gji/ggs105.

Yuan, F., V. Prakash, and T. Tullis (2011), Origin of pulverized rocks during earthquake fault rupture, *J. Geophys. Res.*, *116*, B06309, doi:10.1029/2010JB007721.

Zhang, Q. B., and J. Zhao (2013), A review of dynamic experimental techniques and mechanical behaviour of rock materials, *Rock Mech. Rock Eng.*, doi:10.1007/s00603-013-0463-y.